Molecular Investigation of the Multi-Phase Photochemistry of Fe(III)-Citrate in Aqueous Solution

Christopher P. West[1], Ana C. Morales[1], Jackson Ryan[1], Maria V. Misovich[1], Anusha P. S. Hettiyadura[1], Felipe Rivera-Adorno[1], Jay M. Tomlin[1], Andrew Darmody[2], Brittany N. Linn[1], Peng Lin[1,a], Alexander Laskin[1,3*]

[1]Department of Chemistry, Purdue University, West Lafayette, IN, USA
[2]Department of Aeronautics and Aerospace Engineering, Purdue University, West Lafayette, IN
[3]Department of Earth, Atmospheric & Planetary Sciences, Purdue University, West Lafayette, IN, USA

[a]Now at California Air Resource Board (CARB), 1001 I Street, Sacramento, CA, USA

[*]Correspondence to: alaskin@purdue.edu

Manuscript Submitted to:

Environmental Science: Processes & Impacts

April 8, 2022

Abstract: Iron (Fe) is ubiquitous in nature and found as Fe^{II} or Fe^{III} in minerals or as dissolved ions Fe^{2+} or Fe^{3+} in aqueous systems. The interactions of soluble Fe have important implications on fresh water and marine biogeochemical cycles, which have impacts on global terrestrial and atmospheric environments. Upon dissolution of Fe^{III} into natural aquatic systems, organic carboxylic acids efficiently chelate Fe^{III} to form $[Fe^{III}\text{-carboxylate}]^{2+}$ complexes that undergo a wide range of photochemistry-induced radical reactions. The chemical composition and photochemical transformations of these mixtures are largely unknown, making it challenging to estimate their environmental impact. To investigate photochemical processing of Fe^{III}-carboxylates at molecular-level, we conduct comprehensive experimental study employing UV-visible spectroscopy, liquid chromatography coupled to photodiode array and high-resolution mass spectrometry, and oil immersion flow microscopy. In this study, aqueous solutions of Fe^{III}-citrate were photolyzed under 365 nm light in an experimental setup with an apparent quantum yield of (Φ) ~ 0.02, followed by chemical analyses of reacted mixtures withdrawn at increment time intervals of the experiment. The apparent photochemical reaction kinetics of Fe^{3+}-citrates (aq) were expressed as two generalized consecutive reactions of *Reactants* (*R*) $\xrightarrow{j_1}$ *Intermediates (I)* $\xrightarrow{j_2}$ *Products (P)* with the experimental rate constants of j_1 ~ 0.12 min^{-1} and j_2 ~ 0.05 min^{-1}, respectively. Molecular characterization results indicate that *R* and *I* consist of both water-soluble organic and Fe-organic species, while *P* compounds are a mixture of water-soluble and colloidal materials. The latter were identified as Fe-carbonaceous colloids formed at long photolysis times. The carbonaceous content of these colloids was identified as unsaturated organic species with low oxygen content and carbon with reduced oxidation state, indicative of their plausible radical recombination mechanism at oxygen-deprived conditions typical for the extensively photolyzed mixtures. Based on the molecular characterization results, we discuss the comprehensive reaction mechanism of Fe^{III}-citrate photochemistry and report on the formation of previously unexplored colloidal reaction products, which may contribute to atmospheric and terrestrial light-absorbing material in aquatic environments.

Keywords: water soluble Fe, Fe-carboxylate complexes, photolysis, reactive oxygen species (ROS), semi-solid colloids, liquid chromatography (LC), UV-visible spectroscopy, high resolution mass spectrometry (HRMS), flow microscopy

INTRODUCTION

Iron (Fe) is the most common element on Earth by mass, and found in atmosphere, biosphere, lithosphere, and hydrosphere.[1,2] A majority of Fe is associated with the solid form of rocks of crustal matter in oxygen-deficient settings,[3] whereas soluble and colloidal Fe-containing species are present in oceanic and terrestrial water environments.[4–6] Atmospheric Fe is also naturally abundant in wind-blown mineral dust and other components of particulate matter (PM).[7–13] The interactions, transport, and environmental fate of elemental Fe are vital in the Fe biogeochemical cycle and necessary to sustain life and facilitate important environmental processes.[14,15] The soluble fractions of Fe from Fe-bearing materials[16–18] are mobilized in aquatic environments as a result of various chemical processes such as photolysis and reactions with inorganic acids. Upon dissolution of Fe into aquatic aerobic systems (pH 4 – 8), available organic carboxylic acid components of dissolved organic matter (DOM) efficiently chelate Fe^{3+} ions to form photocatalytically active $[Fe^{III}\text{-carboxylate}]^{2+}$ complexes that promote radical reactions in the aquatic phase. Upon excitation by UV-visible light, the photochemically initiated radical reactions modify the composition of DOM with subsequent effects on optical and physical properties of the environmental aquatic systems.[19]

Molecular-level characterization of reactive components in the Fe-carboxylate photochemical systems is still largely lacking and reported results remain ambiguous. Previous studies utilized optical spectroscopy,[20–24] electrochemistry,[21] and liquid chromatography with optical detection[25] to infer reaction mechanisms and system properties solely from measurements of the bulk solution, but not for the molecular-specific components. However, unravelling the molecular-specific processes leading to the conversion of solid Fe^{III} to soluble Fe^{3+}, Fe^{3+} complexation with carboxylic acids, and the environmental reactions of $[Fe^{III}\text{-carboxylate}]^{2+}$ complexes are still needed for quantitative predictions of Fe^{III}-carboxylate photochemistry in aquatic systems.

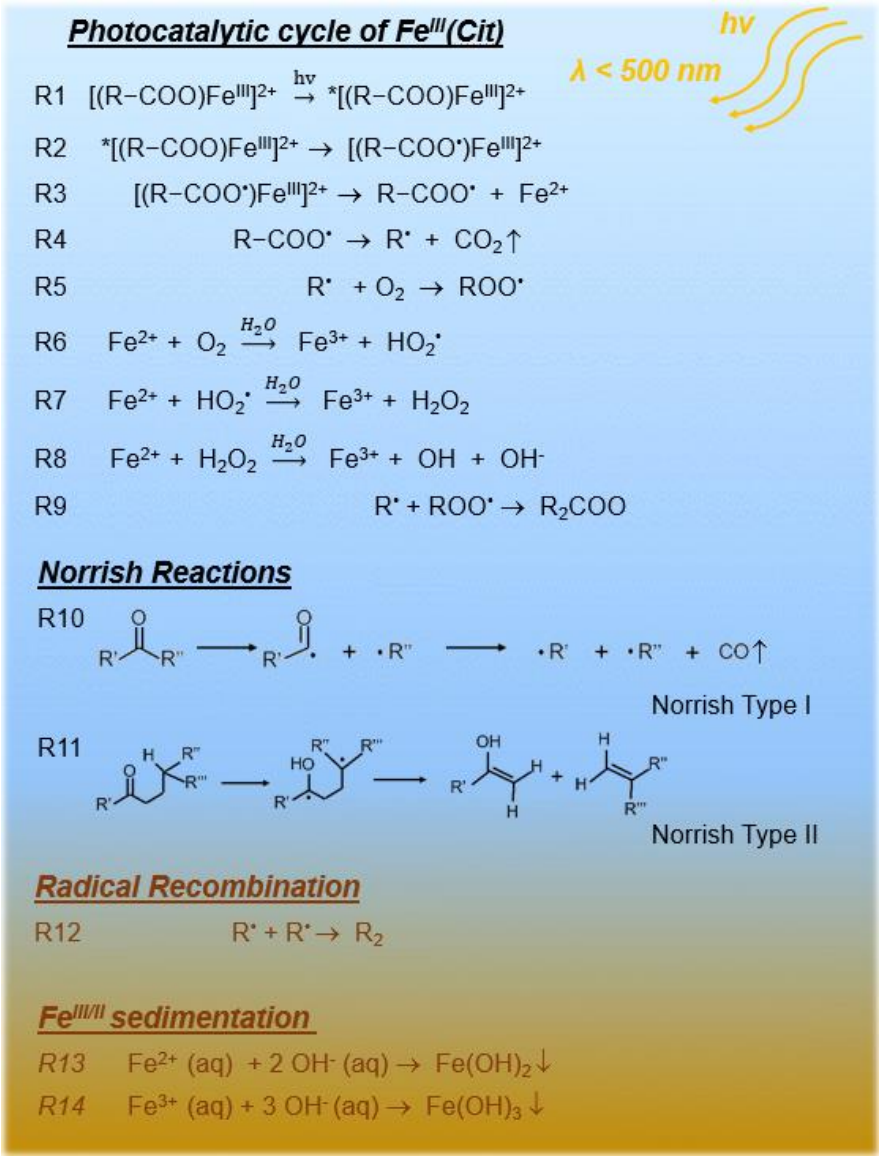

Scheme 1. Reaction sequence of the photo-catalytic redox cycle of Fe^{III}-citrate complex in aquatic environment. R in reactions R1-R5 and R9 corresponds to $-(CH_2CO_2H)_2COH$, ‘R, “R, and “‘R symbols indicate various parts of organic molecules. Mononuclear monocitrate (or 1:1 complex, $[(R\text{-}COO)Fe^{III}]^{2+}$) is shown here as a representative complex in the reaction scheme. Herein, legends of Fe^{2+} and Fe^{3+} refer to dissolved ions, whereas legends of Fe^{III} and Fe^{II} indicate complexation with ligands.

Photoreactive Fe^{III}-carboxylate complexes absorb light at wavelengths below 500 nm, which catalyzes ligand to metal charge transfer (LMCT) reactions, resulting in the reduction of Fe^{III} to Fe^{II} and oxidation of the carboxylate ligands, a process that represents an important sink of organic acids in marine, terrestrial, and atmospheric water.[22,26–31] Scheme 1 summarizes these and other

relevant aquatic reactions. The LMCT process occurs as a result of an electron transfer from the innermost sp^3 orbital of the carboxylate ligand to the metal center, forming $[Fe^{III}\text{-}COO\text{-}R]^{2+*}$-excited state and the $[Fe^{III}\text{-}COO^{\bullet}\text{-}R]^{2+}$ radical complex, as shown in R1-R2.[32] The equivalent lifetime of the intermediate radical complex, determined in previous studies,[24,33–35] was found to be on the order of a few milliseconds, after which it decomposes into Fe^{2+} and $R\text{-}COO^{\bullet}$ as shown in R3. Further reactions of Fe^{2+} and $R\text{-}COO^{\bullet}$ lead to loss of CO_2 as shown in R4, forming alkyl radicals ($R^{\bullet}$).[36–38] Organic peroxy radicals ($RO_2^{\bullet}$) are later formed in the reaction with oxygen (O_2) as shown in R5.[39] Additional reactions of Fe^{2+} ions with dissolved O_2 lead to the formation of reactive oxygen species (ROS)[40–42] such as $HO_2^{\bullet}$, hydrogen peroxide (H_2O_2), and hydroxyl radicals ($OH^{\bullet}$)[43–45] while cycling Fe^{2+} back to Fe^{3+} through the Fenton reaction,[46] as shown in R6-8. The ROS species react further with a variety of organic and inorganic compounds in aqueous solution.[47–50] Subsequently, organic peroxy radicals ($ROO^{\bullet}$) in solution may decompose into smaller organic acid fragments such as oxygenated volatile organic compounds (OVOC), or undergo radical recombination reactions as shown in R9, and R12 resulting in production of larger oligomeric species.

Radical species with carbonyl groups formed after decarboxylation, may undergo Norrish type I and II reactions as shown in R10-11,[51–54] triggering radical chain reactions with O_2 and various organic compounds. Norrish reactions produce carbon monoxide (CO) and carbon-centered radicals (CCRs), such as methyl ($^{\bullet}CH_3$), methyl ketones ($O{=}^{\bullet}C\text{-}CH_3$), and triphenylmethyl ($^{\bullet}C(C_6H_5)_3$), among other radicals.[55] As a result, the dissolved oxygen is effectively consumed, while the CO_2 and CO products are degassed, resulting in oxygen-deficient conditions after prolonged photolysis. As shown in R12, radical recombination forms compounds with lower oxygen content and carbon in reduced oxidation state. These products have much lower solubility than oxygenated organic carbon and therefore may contribute to the buildup of insoluble photomineralization products.[56,57] In addition to the reduced carbon colloids, precipitation of insoluble iron hydroxides,[19] $Fe(OH)_2$ and $Fe(OH)_3$, can take place as shown in R12-13,[58,59] which further contributes to the formation and growth of colloid particles. The insoluble colloids of mixed $Fe(OH)_3$/carbonaceous composition exhibit substantially larger light extinction properties than the water-soluble components in the same mixtures.[60]

127 Multiphase aquatic photochemistry of Fe^{III}-citrate has been studied [20,25,41,55,61,62] as a laboratory
128 proxy for the environmental Fe^{III}-carboxylate systems. To date, the production and detection of
129 gas-phase OVOC upon photolysis of Fe^{III}-secondary organic aerosol proxies containing carboxylic
130 acids in flow reactors[63] have been investigated. Other studies reported changes in the
131 microphysical properties, chemical composition, and ROS capacity of viscous Fe-citrate particles
132 levitated in electrodynamic balance and probed by spectromicroscopy after exposure to UV
133 light.[41,55] These studies[41,55] demonstrated significant photochemical degradation after 24 hours of
134 irradiation, resulting in ~ 80% mass loss of particles due to degassing of CO_2 and OVOC, and slow
135 uptake/molecular diffusion of O_2 in the particle phase, consistent with reactions R1-8 of Scheme
136 1. The combination of these studies provides surface and physical property characterization
137 results. However, molecular-level composition, optical properties, and extent of the photochemical
138 reactions occurring in the condensed phase are still insufficiently investigated. This knowledge
139 gap precludes quantitative predictions of the photocatalytic processing for Fe-carboxylate systems
140 and their consequences on environmental systems.
141
142 In this work, the chemical composition and optical properties of aqueous Fe^{III}-citrate
143 photocatalytic components were investigated using high-performance liquid chromatography
144 coupled to a photodiode array and high-resolution mass spectrometry (HPLC-PDA-HRMS)
145 detectors,[64–71] and were further evaluated with direct infusion (DI) HRMS chemical analysis.[66,70,72]
146 Colloidal products produced during photolysis reactions were imaged with *in situ* oil immersion
147 flow microscopy. Multi-modal datasets from these complementary techniques provide a unique
148 experimental description of various stages of Fe^{III}-citrate photochemistry, elucidate individual
149 components of this reacting system, determine mechanistic insights, and quantify environmental
150 parameters affecting the Fe^{III}-carboxylate photochemistry.
151
152
153 **EXPERIMENTAL METHODS**
154
155 **Sample Preparation** 10mM stock solutions of ferric citrate ($C_6H_5O_7Fe$, 16.5 – 18.5 % Fe basis,
156 BioReagent, CAS: 3522-50-7; Sigma Aldrich Inc.) and of citric acid ($C_6H_8O_7{\cdot}H_2O$; 99% purity,
157 Mallinckrodt Inc.) analytical blank for HPLC analysis were prepared in 100mL borosilicate
158 volumetric flasks using 18.1 MΩ cm^{-1} Milli-Q ultrapure water. The stock solutions were wrapped

159 in aluminum foil (Fisher Inc.) and stored in a refrigerator at ~5 °C. The ferric citrate stock solution
160 were further diluted to ~ 9.0 x 10^{-5} M (90 μM) in the ultrapure water and were set to equilibrate
161 for ~ 2-24 h in the dark prior to chemical characterization, as recommended in the literature.[73,74]
162
163 **Photochemical Experiments and Optical Spectroscopy measurements.** A custom-built
164 photolysis reactor setup employing a constant wavelength light emitting diode (LED) that emits
165 blue light at ~ 365 ± 9 nm (Model: M365LP1; Thor Labs Inc.) was placed ~ 20 cm above the
166 sample compartment (qpod2e, Quantum Northwest Inc.). The sample was placed in a 10 mm
167 quartz cuvette (Vernier Inc.). The mounted UV- LED optics and adjusted collimator lens in these
168 experiments resulted in an illuminated cross-sectional area of 0.78 ± 0.05 cm^2. All experiments
169 were conducted at room temperature (~ 24-26 °C), and temperature was monitored throughout the
170 reaction. Additional details of the experimental methods and instrumentation parameters are
171 described in Figure S1 (Appendix A of the SI file). UV-Visible absorption spectra of the
172 photolyzed solutions were acquired using a USB 2000 UV-Vis-NIR (Ocean Optics Inc.) fiber
173 optic spectrophotometer. The samples were analyzed over the 200 – 900 nm wavelength range
174 employing 20 ms integration time, 6 scans to average, and boxcar width of 4.
175
176 The spectral flux of the LED radiation (F_{LED}) experienced by the samples was experimentally
177 determined by the chemical actinometry method using a 1 mM solution of potassium ferrioxalate
178 ($K_3[Fe(C_2O_4)_3]$; Sigma-Aldrich) in 0.05M sulfuric acid (Honeywell Inc.), described by Lehóczki
179 et al., 2013.[75] The decrease in absorption of ferrioxalate ($\varepsilon_{Fe\text{-}Ox}$ ~ 312 ± 2 L mol^{-1} cm^{-1} at 390 nm)[75]
180 as a function of irradiation time was measured and converted to the F_{LED} ~ 3.85 x 10^{15} photons
181 cm^{-2} s^{-1} at 365 nm, with a quantum yield, Φ ~ 1.26. Description and results of flux calculations
182 is provided in Appendix B and Figure S2 of the SI file.
183
184 **Quantitation of Dissolved Fe^{2+}** Quantification of Fe^{2+} concentrations in irradiated solutions
185 employed colorimetric tests with 1,10-phenanthroline ($C_{12}H_8N_2$; ≥ 99% purity, Sigma-Aldrich
186 Inc.), whereby dissolved Fe^{2+} ions and 1,10-phenanthroline form a red-orange complex that
187 absorbs visible light at ~ 510 nm.[76,77] For analysis, 0.5 mL of analyte sampled at 0, 5, 20, 40, 80,
188 and 120 min irradiation time were mixed with 1.5 mL of 5mM 1,10-phenanthroline and filled to
189 3mL with 1mL of 18.1 MΩ cm^{-1} Milli-Q ultrapure water. Quantitative [Fe^{2+}] measurements were

190 performed in triplicate to establish reproducibility. For calibration, chemical standards of Fe^{II}
191 perchlorate hydrate ($Fe(ClO_4)_2 \cdot H_2O$; 98% purity, Sigma Aldrich Inc.), ranging from 1-90 μM
192 concentrations, were mixed with 5 mM 1,10- phenanthroline, and their respective absorbances
193 were measured and recorded via a seven-point calibration curve (Figure S3 in SI file). The limit
194 of detection (LOD) and molar absorptivity (ε_{510nm}) obtained from calibration measurements in this
195 study are ~ 2.3 μM and ~ 7400 L mol^{-1} cm^{-1}, respectively.
196
197 **Chemical Characterization** 300 uL aliquots of the initial (non-photolyzed) and irradiated
198 mixtures were withdrawn from the cuvette containing 3 mL of experimental solutions at 0, 5, 40,
199 80, and 120 min. Components of the Fe-citrate mixtures were characterized using a Vanquish™
200 high performance liquid chromatography (HPLC) system equipped with an autosampler, a
201 photodiode array (PDA) detector, and a Q Exactive™ HF-X Orbitrap mass spectrometer
202 interfaced with an IonMAX source which housed a heated electrospray ionization (HESI) probe
203 operated in negative ion mode (all from Thermo Scientific Inc.). Chemical constituents were
204 separated on a zwitterionic hydrophilic interaction liquid chromatography (ZIC-HILIC) column
205 (Synchronis™, 2 mm × 150 mm, 5 μm particles, 100 Å pore size, Thermo Inc.). ZIC-HILIC
206 column can retain ionic and highly polar, hydrophilic compounds, through liquid-liquid
207 partitioning, electrostatic interactions, and hydrogen bonding,[78] which cannot be separated on
208 conventional reversed-phase LC columns.[79] The incorporation of a zwitterionic HILIC stationary
209 phase is particularly applicable for retention of highly polar species such as charged metal-organic
210 complexes (i.e. Fe-citrate, Fe-malate, and Fe-siderophores).[80–85] A multistep gradient elution was
211 performed at a flow rate of 0.2 mL min^{-1} using a binary mobile phase-buffer system: (A) LC/MS-
212 grade water (Optima™, Sigma Aldrich Inc.) with 10 mM ammonium acetate buffer (v/v) and (B)
213 LC/MS-grade methanol (Optima™, Sigma Aldrich Inc.) with 10 mM ammonium acetate buffer
214 (Sigma Aldrich Inc.). The buffer pH for all LC experiments was held within 5.2 - 6.8 to preserve
215 the metal-ligand equilibria.[84] Elution proceeded as follows: 0−3 min held at 95% B, 3−7 min linear
216 gradient to 20% B, 7−15 min held at 20% B, 15-19 min linear gradient to 95% B, and re-
217 equilibration period at 19-57 min held at 95% B to prepare for the next injection in the sequence.
218 The autosampler compartment temperature where sample vials were stored was held at 15°C. The
219 column temperature was held at 35°C and an injection volume of 15 μL (~258 ng of injected
220 organic analyte) was used. No additional sample preparation was performed, and samples were

221 directly withdrawn and analyzed from the irradiated solutions. The UV−visible absorption spectra
222 of LC-separated components were measured using the PDA detector equipped with a deuterium
223 light-source and 1.0 cm fused-silica LightPipe™ flow cell, with a wavelength range of 200−680
224 nm (3D Field spectra), a scan rate of 20 Hz, and λ ± 4 nm spectral resolution. The following
225 conditions were used for the HESI source operation in the HPLC experiments: 40 °C probe heater
226 temperature, 100 °C capillary temperature, 30 units of sheath gas flow, 10 units of auxiliary gas
227 flow, 0 units of sweep gas flow, 3.5 kV spray potential, and a funnel RF level of 30. A method
228 blank was used for all LC-PDA-HRMS experiments, corresponding to 90 μM citric acid standard.
229 Analyzed samples were ionized in the negative ionization mode and HPLC-PDA-ESI(−)/HRMS
230 datasets were acquired using Xcalibur software (Thermo Inc.). The HRMS was operated at *m/Δm*
231 240,000 resolving power at 200 m/z, at a scan rate of 1.5 Hz in the full MS scan mode of 100 –
232 1300 m/z range. Custom mass calibration was performed using commercial calibration solutions
233 (Thermo Scientific, PI-88324) ionized in the negative ESI mode.
234
235 Additionally, two sets of HRMS experiments were performed by (1) directly infusing (DI-HRMS)
236 Fe^{III}-citrate solutions photolyzed at 0, 5, 40, 80, and 120 minutes (Exp. 1) in the negative mode to
237 screen for overall water soluble Fe^{III}-citrate components and their photochemical products, and
238 (Exp. 2) to specifically probe components of the unreacted and 120 min irradiated sample for
239 colloidal/carbonaceous products dissolved in 1 mL of a mixture of organic solvents (2:2:2:1 v/v%,
240 acetonitrile (ACN)/dichloromethane (DCM)/ hexanes/ toluene), the '*org-mix*' hereafter, in the
241 positive ion mode. After this step, colloidal mixture underwent dissolution and intentional
242 disruption assisted by ultrasonication for ~ 40 min, followed by filtering using 0.45 μm PTFE
243 syringe filter cartridges (Thermo Inc.), and solvent evaporation on the TurboVap (Biotage Inc.) at
244 1.5 L min^{-1} flowrate to ~ 1 mL level of remaining water solvent. 20% methanol was added before
245 DI-HRMS as recommended in the literature.[73,74] DI-HRMS experiments were conducted using
246 similar MS tune conditions described above at 5 μL min^{-1} injection flow rate for the water-soluble
247 fraction and slightly modified tune parameters for analysis of the colloid components dissolved in
248 the *org-mix*. For the analysis of colloid components dissolved in *org-mix*, the sheath, auxiliary gas
249 flow, funnel RF-level, capillary, and source heater temperature were adjusted to 30, 10 arbitrary
250 units, 80, 250 °C and 100 °C, respectively to allow for efficient droplet desolvation, ionization and
251 detection of larger molecular weight species. In Exp. 1 and Exp. 2 mass spectra were acquired in

negative and positive modes, respectively. Targeted MS^2 experiments were performed for structural characterization of selected components of the Fe-citrate mixtures in the negative mode. Additional details of DI-HRMS and targeted MS^2 experiments are described in Appendix C of the SI file.

Data Processing & Analysis. Raw Xcalibur data files were background-subtracted prior to data processing and analysis to remove any signal attributed to the method blank. The HPLC-ESI/HRMS datasets were batch-processed with customized java script in the open-source software, MZmine 2 (v. 2.51, http://mzmine.github.io/), to perform data preprocessing, chromatogram construction, peak deconvolution, peak smoothing, peak alignment, peak annotation, and analyte identification with the CAMERA R-package (Bioconductor R-repository).[86,87] The ADAP chromatogram builder[88] was used to reconstruct extracted ion chromatograms (EIC) and obtain the output chromatographic feature list, using a minimum peak height of 10^3, LC peak duration of 0.6 min, and mass tolerance of 0.001 m/z. The combined software algorithm identifies the analyte species, assuming the annotated ions in the range 100 – 1300 m/z were formed by the loss of a proton in the ESI(–) mode. The detected peaks identified by MZmine 2 were cross evaluated using the Xcalibur software (Thermo Scientific Inc.), thus eliminating erroneous formula assignments occasionally made by the algorithm. In addition, the overall screenings of the Fe-containing peaks detected in the bulk samples were performed in DI-ESI(–/+)/HRMS experiments. Obtained data sets were extracted with the DeconTools AutoProcessor software developed at the Pacific Northwest National Laboratory (v. 1.0; http://omics.pnl.gov/software/)[89] and processed using custom Excel macros (Microsoft Inc.) developed for mass alignment, background subtraction, and ^{13}C isotope filtering. Formula assignments were assisted with grouping of the homologous species assigned based on first-order (CH_2) and second-order (CH_2, H_2) Kendrick mass defects, followed by the group-representative formula assignments[90] using the MIDAS molecular formula calculator (v 1.1; http://nationalmaglab.org/user-facilities/icr/icr-software). Isotope distributions of Fe-containing peaks were compared with results obtained from mass spectral isotope distribution simulator software, IsoPro (v. 3.0; https://sites.google.com/site/isoproms/), as well as isotope peak scanner function in MZmine 2 to search for m/z and intensity distribution of a calculated isotope pattern within the feature list. The following constraints were applied for all formula assignments: $C_{1\text{-}60}$,

H_{1-100}, O_{0-22}, Fe_{0-5}, charge ≤ 2, and mass tolerance of ± 3 ppm. MS peaks with a signal to noise (S/N) ratio ≥ 5 were only considered for this analysis. Double-bond equivalent (DBE) values of the neutral assigned species were calculated using the following equation[91]:

$$\mathrm{DBE} = C - H/2 + N/2 + 1. \qquad (1)$$

Throughout the manuscript, all molecular formulas discussed in the text below correspond to neutral molecules in case of $C_xH_yO_z$ composition and to ions in case Fe-containing organic compounds, superscripted by their corresponding charges.

Calculation of Mass Absorption Coefficient (*$MAC_{\lambda,OM}$*)

Optical Measurements of Bulk Solutions. The absorption spectra presented in this work are in the units of wavelength-dependent mass absorption coefficient ($MAC(\lambda)_{bulk}$ eq. 2),[92] which is calculated from log base-10 absorbance ($A_{10}^{solution}$) of the aqueous solution with organic mass (OM) concentration (C_{mass}, g m^{-3}), and optical path length (b = 0.01 m).

$$MAC(\lambda)_{bulk}(\mathrm{m^2\ g^{-1}}) = \frac{A_{10}^{solution}(\lambda) \times ln\,(10)}{b \times C_{mass}} \qquad (2)$$

Whereas C_{mass} is calculated as mass concentration of the organic component (i.e., citrate, $C_6H_5O_7^{3-}$). Therefore, C_{mass} in the case of 90 μM Fe-citrate ($C_6H_5FeO_7$) is ~ 17.02 g m^{-3}. The calculation assumes that total OM value does not change in the reacted Fe-citrate mixtures. This assumption, however, underestimates $MAC(\lambda)_{bulk}$ values as decarboxylation reactions produce CO_2 and small oxygenated VOC products, which can volatilize from the solution, therefore reducing OM concentration in the reacted solutions. The open headspace in the experimental setup leads to evaporation and degassing of VOC products from photoreacted solutions. Thus, the computed $MAC(\lambda)_{bulk}$ values reported here should be viewed as the lower estimates. The wavelength dependence of $MAC(\lambda)_{bulk}$ expressed through absorption Ångström exponent (*AAE*) was assumed using the following formula:

$$MAC(\lambda)_{bulk} = k \times \lambda^{-AAE} \quad (3)$$

AAE values were derived by computing the slope of the linear dependence of $MAC(\lambda)_{bulk}$ versus wavelength plotted on a ln-ln scale, while *k* is the imaginary part of the refractive index.[93] For the analytes of this study, we calculate *AAE* over 250-450 nm spectral range.

Photodiode Array (PDA) Optical Measurements of Solution Components. The $MAC(\lambda)^{PDA}$ values derived from integrated UV-vis records obtained in LC-PDA measurements and corresponding to the total light absorption in each of the aliquot samples were computed using eq. 4.[94,95]

$$MAC(\lambda)_{\Sigma}^{PDA}(m^2\ g^{-1}) = \frac{A(\lambda)_{\Sigma}^{PDA}(\mu AU) \times \Delta t \times F \times ln\,(10)}{b\,(cm) \times m_{inj} \times 10} \quad (4)$$

In this analytical expression, $A(\lambda)_{\Sigma}^{PDA}$ is the optical absorbance from PDA detector recorded at wavelength λ over the period of LC separation (Σ = 0 – 12 min), including the unretained fraction eluting at 0 – 3 min. Δt is the elution time range (12 min); *F* is the LC flow rate (0.2 mL min^{-1}); *b* is the optical pathlength of the PDA flow cell (1 cm), and m_{inj} is the injected mass (258 ng) of OM analyte. The coefficient 10 accounts for the combined conversion of μAU into AU, cm^3 into m^3, cm into m, and ng into g.[94,95]

The relative fractional contributions of $MAC(\lambda)_{i}^{PDA}$ attributable to each of the individual LC-separated features (*i*) in the analyzed samples were computed using equation 5.

$$MAC(\lambda)_{i}^{PDA} = MAC(\lambda)_{\Sigma}^{PDA} \times \left(\frac{A(\lambda)_{i}^{PDA} \times \Delta t_i}{A(\lambda)_{\Sigma}^{PDA} \times \Delta t_{\Sigma}}\right) \quad (5)$$

where $A(\lambda)_{i}^{PDA}$ (μAU) is the averaged UV-visible absorbance of the individual feature *i* and Δt_i (min) is its time duration. All UV-visible absorption data presented here were processed and exported using custom MATLAB (R2018a, MathWorks Inc., USA) scripts developed in our group. In our study, we report on the molecular composition of the Fe-Citrate reacting mixture and specify the individual $MAC(\lambda)_{i}^{PDA}$ contributions as a function of reaction time. From there, we

342 incorporate a 'bottom up' approach to interpret optical transformations of the bulk Fe-citrate
343 material in terms of a practical concept of simplified sequential reactions where first-order reaction
344 kinetics are quantified based on computed $MAC(\lambda)_{bulk}$ values.
345
346 ***In Situ* Flow Microscopy Detection of Colloids.** 300 µL of the unreacted, 5 min, 40 min, 80 min,
347 and 120 min irradiated solutions sampled from same cuvette were analyzed *in situ* using a
348 FlowCam® Nano instrument (Yokogawa Fluid Imaging Technologies Inc.) operated with the
349 VisualSpreadsheet 5.6.26 software (Fluid Imaging Technologies). The FlowCam® Nano
350 instrument uses oil immersion flow microscopy[96,97] to focus and image particles as they pass
351 through a flow cell. Prior to imaging experiments, the instrument was autofocused with NIST
352 Traceable Polymer Microspheres standard (Lot No: 247697) with known diameter (*Dp*) of 0.702
353 $\pm$ 0.006 µm. The background intensity in all experiments were measured within the 173-178 A.U.
354 range. The instrument parameters are as follows: x40 objective lens, 0.1 µm distance to nearest
355 neighbor, threshold dark/light 18/18, 1 close hole (iterations), 60 µm flow cell depth, 500 µm flow
356 cell width, 0.3 mL sample volume, 0.025 mL min^{-1} sampling flow rate, auto image rate of 137
357 frames s^{-1}, sample run time 12.00 min, particle size range 0.3 – 60 µm when operated in relative
358 count mode. Particle number concentrations were determined using count calibrated mode with
359 the instrument default settings of 0.1 µm distance to nearest neighbor, threshold dark/light 20/20,
360 1 close hole (iterations), 60 µm flow cell depth, 500 µm flow cell width, 0.3 mL sample volume,
361 0.025 mL min^{-1} sampling flow rate, auto image rate of 137 frames s^{-1}, sample run time 12.00 min,
362 and a particle size range 0.3 – 60 µm. After each measurement, the microfluidic system was rinsed
363 with 0.20 µm filtered Windex® or 0.1% Liquinox surfactant soap in water (Optima™, Sigma
364 Aldrich Inc.) followed with a rinse of pure water. Diameters reported from this measurement are
365 equivalent size diameter.
366
367 **RESULTS AND DISCUSSION**
368
369 **Photolysis of the Fe^{III}-Citrate aqueous system.** Figure 1a shows the $MAC(\lambda)_{bulk}$ absorption
370 spectra of the Fe^{III} citrate system measured at selected time intervals during the photolysis
371 experiment. Figure 1b further illustrates evolution of the same $MAC(\lambda)_{bulk}$ spectra but shown as a
372 continuing progression recorded at 5 s intervals using transient optical spectroscopy. The plots
373 show very rapid decrease of the *MAC* values over the first ~ 5 min of the irradiation, followed by

gradual increase over next ~100 min of the experiment. From the beginning of the reaction and during the initial decrease, $MAC(\lambda)_{bulk}$ spectra show a significant drop in their *AAE* values (from 6.86 to 4.21) but remain featureless. In contrast, over the follow-up increase period, $MAC(\lambda)_{bulk}$ spectra consistently show buildup of an absorption feature at 256 nm and *AAE* values of the spectra show only moderate change (from 4.21 to 3.62). Figure 1c shows a time-resolved record of MAC_{256nm} values over the entire irradiation time, indicating a reaction trend consistent with the formal kinetics of two first-order consecutive reactions of *Reactants (R)* $\overset{j_1}{\rightarrow}$ *Intermediates (I)* $\overset{j_2}{\rightarrow}$ *Products (P)*. Figure 1c shows kinetic modeling results using this apparent first-order kinetic scheme, featuring relative concentration profiles of *R, I,* and *P* components. Details of the kinetic model are described in Appendix D of the SI file. The pH of the initial ferric citrate solution was measured to be 6.7 and changes slightly to 6.52 in the 120 min photoreacted sample. Therefore all photolysis reactions were reproduced within the narrow pH range of this study.

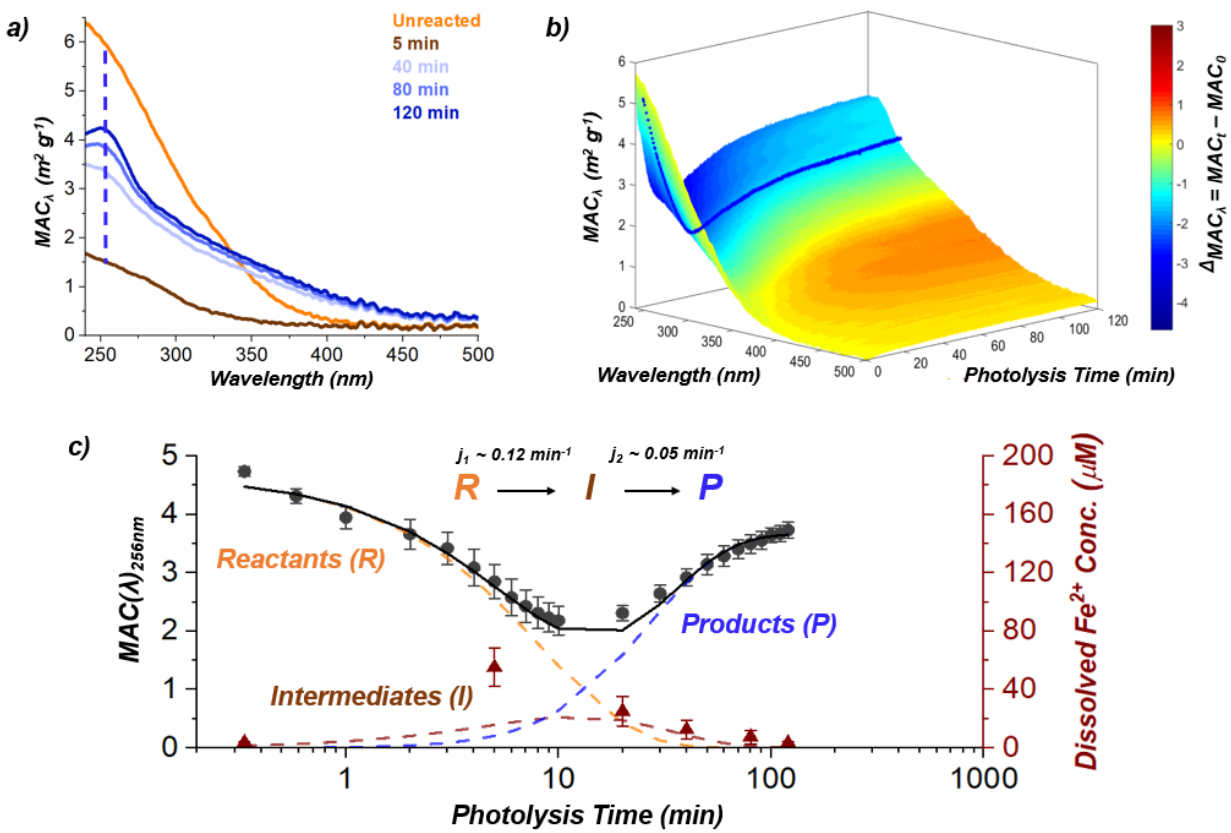

Figure 1. a) *MAC(λ)* spectra of 90 μM Fe^{III}-citrate (1:1 M:L) solution undergoing photochemical transformations recorded at t = 0, 5, 40, 80, 120 min of irradiation time. Dashed line indicates absorption at 256 nm b) 3D *MAC(λ)* plot illustrating the same transformations recorded at high time resolution (5s) in

390 a separate experiment. The x, y, and z-axis represent the absorbing wavelength (nm), MAC_{λ}, and photolysis
391 time (min), respectively. Colormap is scaled by the difference in *MAC* units ($^{\Delta}MAC = MAC_t - MAC_0$). 2D
392 contour line indicating transient absorption at 256 nm. c) Single-wavelength MAC_{256nm} experimental data
393 of the Fe^{III}-citrate photolytic time-resolved transformations (black circles, error bars represent standard
394 deviation of 3 replicated measurements). The reaction extent is modeled (dashed lines) using Apparent First
395 Order Kinetics for a formal mechanism of two consecutive irreversible reactions: *Reactants* (*R*) →
396 *Intermediates* (*I*) → *Products* (*P*). Right Y axis of figure 1c shows the overall concentrations of Fe^{2+} ions
397 (brown triangles) measured in the solutions at 0, 5, 20, 40, 80, 120 min of irradiation time.

398 The $MAC(\lambda)_{bulk}$ spectrum of the original Fe^{III}-citrate solution (Fig 1a, orange trace) exhibits
399 characteristic tailing that extends to the visible region of the spectrum. These absorption
400 characteristics are very consistent with previous literature reports,[21,22,61,98,99] and are similar to
401 optical characteristics exhibited by other Fe^{III} – carboxylate complexes.[34,100–102] Spectral
402 characteristics of Fe^{II}-ligand species presented here and in the later text may be attributed to the
403 λ_{max} at ~ 256 nm. Previous study[103] report the UV-vis spectra of Fe^{II}- tannic acid complexes at
404 acidic pH absorbing closer to 260 nm, while Fe^{II}-cationic complexes in aprotic solutions exhibit a
405 unique and narrow λ_{max} at 262 nm.[104] The photochemical mechanism of the Fe^{III}-citrate system
406 (scheme I) explains the evolution of the $MAC(\lambda)_{bulk}$ spectra observed in our experiment.
407 Specifically, the initial photolysis of Fe^{III}-citrate (*R* → *I* reactions) proceeds through rapid ligand to
408 metal charge transfer (LMCT) excitation,[105] reducing Fe^{3+} to Fe^{2+} and dissociating and oxidizing
409 the citrate-radical pair.[31] Reduced Fe^{2+} products exist as intermediate species; they are oxidized
410 back to Fe^{3+} (*I* → *P* reactions) at the longer photolysis times in the presence of ROS species and
411 dissolved oxygen. The formal kinetics and modeled curves describing relative fractions of *R, I,*
412 and *P* components in the photoreacting system shown in Figure 1c indicate a net apparent effect
413 of reactions similar to R1-9 (Scheme 1). To validate our assumption that *I* products are indeed
414 associated with Fe^{II} intermediates, we measured dissolved [Fe^{2+}] concentrations at selected
415 irradiation times. The Fe^{2+} concentration is low in the unreacted sample (3.8 μM), which is close
416 to the limit of detection (~2.3 μM). As the photolysis progresses to 5 min, the averaged
417 concentration of dissolved Fe^{2+} increases to 55.3 μM, then gradually decreases to 25-12 μM at 20-
418 40 min and to 7-3 μM at 80-120 min, respectively. Figure 1c shows that overall concentrations of
419 Fe^{2+} ions in the solutions (brown triangles) agree well with the modeled time-resolved profile of
420 the intermediate products *I* (brown dashed lines). The processes influencing [Fe^{2+}] production are

421 related to (1) dissociation of citrate ligand from Fe^{III} center and reduction following LMCT as
422 previously mentioned.[31,105] (2) The reactions and rate of reactions of available ROS (i.e. H_2O_2, O_2,
423 and HO_2) in the solution with dissolved Fe^{2+} and (3) speciation of Fe(II) in the aqueous solution at
424 the higher pH (~6.5 - 6.7) ranges where peroxides react with photoreduced Fe^{2+} and re-oxidize
425 back to Fe^{3+}, significantly faster than at the lower pH conditions in separate studies.[43,62,106]

426 The apparent quantum yield, Φ of the generalized photochemical decomposition of R (Fe^{III}-citrate
427 reactant) was calculated based on the observed number of reacted Fe^{III}-citrate molecules divided
428 by the number of photons to which the experimental solutions were exposed. The latter was
429 calculated based on the photon flux measured in the actinometry experiments (Appendix B in SI
430 file). The calculated apparent Φ is ~ 0.02, which is only ~10% of the intrinsic Φ values reported
431 in the range of ~ 0.16 – 0.30 for Fe^{III}-carboxylates.[25,61] Lower values of the apparent Φ are a
432 combined result of additional absorbance and scattering by other components in the reaction
433 mixture, which evolve over the reaction time. Therefore, apparent first-order reaction rates of j_1=
434 0.12 min^{-1} and j_2= 0.05 min^{-1} obtained from the formal kinetic modeling need to be considered as
435 specific to our experimental conditions. Details of the kinetic model are described in Appendix E
436 of the SI file. For the extrapolations of kinetic data to experiments external to our study, the
437 apparent rates and the apparent Φ need to be considered together, scalable to the relevant Φ values
438 determined in the corresponding experiments.

439 **Molecular Characterization of the Irradiated Samples.** Figure 2a illustrates HPLC-PDA
440 experimental results showing separated components of Fe^{III}-citrate solutions irradiated for 0, 5, 40,
441 80, and 120 min. For our analysis, the major separated absorbing components eluted between 0 –
442 3 min RT unretained period and 3 – 12 min RT for weakly to strongly retained species. Therefore,
443 we discuss those identified within these two LC ranges. The individual features are labeled
444 accordingly in each of the respective panels as reactants (R_i), intermediates (I_i), and products (P_i),
445 with their respective coloring schemes from Figure 1c describing the $R \rightarrow I \rightarrow P$ progression. In
446 total, 31 individual HPLC-PDA features (~ 95% of all features) are detected and identified in 5
447 irradiated samples based on the correlative assessment of HPLC-PDA and HPLC-ESI(–)/HRMS
448 records. Table 1 includes a list of separated features and proposed structures commonly grouped
449 with R_x, I_y, and P_z components, whereas the full list of separated features with corresponding
450 retention times, UV-vis spectra, and HRMS information are reported in Table S1 of the SI file.

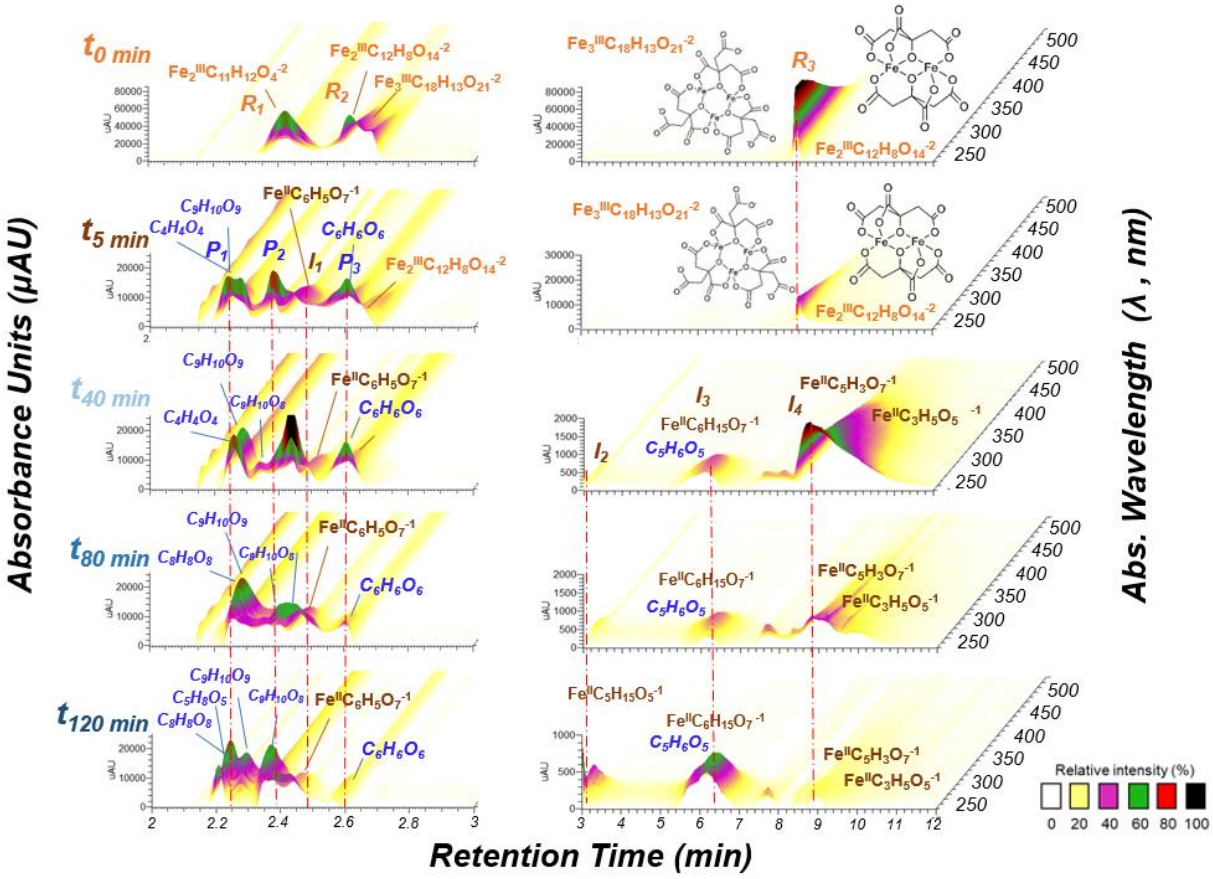

Figure 2. HPLC-PDA chromatograms of individually separated components formed in irradiated Fe^{III}-citrate solutions at 0, 5, 40, 80, and 120 min. The x-axis is retention time, y-axis is UV–vis absorbance and z axis is wavelength. Color indicates relative absorbance as depicted by the color map at the bottom. Assigned formulas corresponding to organic compounds (CHO-) recorded here as neutral molecules, whereas Fe-organic compounds denoted as corresponding ions.

The molecular components of the unreacted solution show three HPLC-PDA features at 2.4, 2.7and 8.7 min RT, marked as R_1, R_2 and R_3, respectively. Analysis of the corresponding HRMS datasets revealed deprotonated ions $[M\text{-}H]^-$ of $^{56}Fe_2^{III}C_{12}H_8O_{14}^{-2}$, $^{56}Fe_3^{III}C_{18}H_{13}O_{21}^{-2}$, $^{56}Fe_3^{III}C_{18}H_{15}O_{22}^{-2}$, and $^{56}Fe_3^{III}C_{12}H_{10}O_{14}^{-2}$ eluted at the corresponding time of R_2 and R_3, which collectively represent the dinuclear dicitrate (Fe_2Cit_2), trinuclear tricitrate (Fe_3Cit_3 & Fe_3Cit_3O), and trinuclear dicitrate (Fe_3Cit_2) complexes, respectively.[73,74,84] The R_1 feature corresponds to $[M\text{-}H]^-$ of $^{56}Fe_2^{III}C_{11}H_{12}O_4^{-2}$. Detection of this Fe-containing peak did not correspond to any of the Fe_xCit_y complexes observed here, nor in previous studies. It is assumed that this is likely a chemical impurity of the Fe^{III}-citrate chemical used in the study. Detection of their characteristic ^{54}Fe

466 isotopes in the integrated MS spectra explicitly confirmed molecular assignments of the Fe-
467 containing ions. Extracted ion chromatograms of the Fe^{III}-citrate complexes overlaid with the LC-
468 PDA chromatographic peaks are illustrated in Figure S4 of the SI file. Details of DI-ESI(-)/HRMS
469 and ESI-MS^2 characterization of all Fe-containing peaks in the unreacted sample are described in
470 Figures S5, S6 and Table S2 of the SI file. After 5 min of photolysis, all *R* features decrease
471 substantially, indicating their lower concentrations. We estimate the summed concentration of
472 Fe^{III}-citrate complexes (R_2 and R_3) from the HPLC-PDA measurement based on the literature
473 reported molar extinction coefficient at λ = 365 nm (ε = 900 L mol^{-1} cm^{-1})[107] to be ~ 78.4 and 1.4
474 μM for 0 and 5 min samples, respectively. Considering that this concentration of the Fe^{III}-citrate
475 complexes in the unreacted mixture is lower than concentration of the dissolved Fe^{III}-citrate salt
476 (~ 90μM), the remaining 11.6 μM likely corresponds to un-complexed/un-dissolved $[Fe]^{3+}$,
477 $[citrate]^{3-}$ ions, and surface-bound Fe^{III}-citrate complexes on the high surface area iron oxide (i.e.
478 FeOOH) colloids in the solution.[108] At the relevant Fe concentrations used in this study, formation
479 of insoluble iron oxide colloids precipitated in the aqueous solution at the higher pH setting
480 form.[109] For mechanistic interpretation of Fe(III)-citrate photochemical degradation discussed
481 here, special consideration of multi-phase photoreductive dissolution processes of colloidal
482 surface-bound Fe^{III}-citrate and other Fe-organic complexes in the aqueous solution should be
483 accounted for.[108,110–112] The photodegradation of oxide bound Fe^{III}-citrate complexes lead to
484 dissolution of Fe^{III}-citrate, followed by Fe(III) reduction and immediate release of soluble Fe^{2+} and
485 citrate from colloid to the aqueous solution.[108] Overall, photodegradation of the soluble and surface
486 bound Fe^{III}-citrate complexes initiated through LMCT reactions[31] R1-R4 (Scheme 1) is very fast,
487 resulting in rapid reduction of Fe^{III} to Fe^{II} over the first 5 min of photolysis. *R* components were
488 not detected in the samples collected at longer irradiation times.

489

Table 1: Summary table of identified components in LC-PDA-HRMS datasets.

ID	*RT (min)*	*UV-Vis Spectrum*	*Exp. m/z* (-)ESI	*Chemical Formula*	*Mass Error (ppm)*	*Proposed Structure & Description*
			Reactants (R_i)			
R_1	2.3	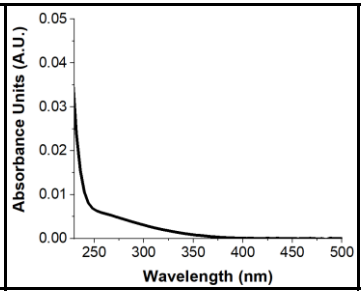	159.972	$Fe_2^{III}C_{11}H_{12}O_4^{-2}$	1.875	
R_2	2.6	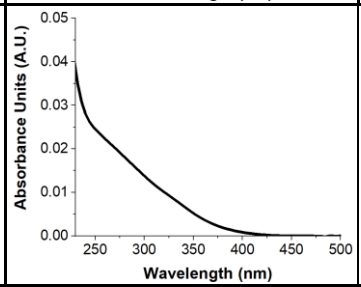	366.401 375.406 243.931 488.870 271.899	$Fe_3^{III}C_{18}H_{13}O_{21}^{-2}$ $Fe_3^{III}C_{18}H_{15}O_{22}^{-2}$ $Fe_2^{III}C_{12}H_8O_{14}^{-2}$ $Fe_2^{III}C_{12}H_9O_{14}^{-1}$ $Fe_3^{III}C_{12}H_{10}O_{14}^{-2}$	0.689 0.533 0.152 0.466 0.345	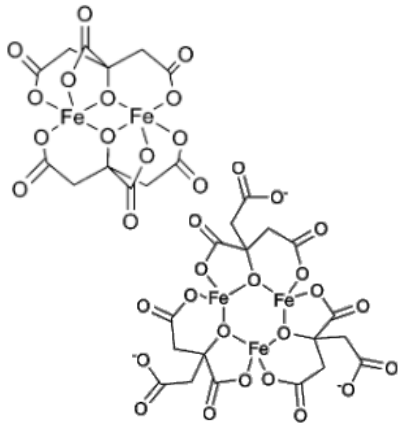 *Iron(III)-citrate (Fe:Cit) complexes based on previous literature, Fe isotope distribution, and optical signals/UV-vis spectra.*[74,113]
R_3	8.4	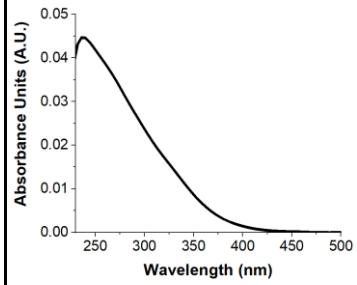	366.400 375.406 243.931 488.870 271.898	$Fe_3^{III}C_{18}H_{13}O_{21}^{-2}$ $Fe_3^{III}C_{18}H_{15}O_{22}^{-2}$ $Fe_2^{III}C_{12}H_8O_{14}^{-2}$ $Fe_2^{III}C_{12}H_9O_{14}^{-1}$ $Fe_3^{III}C_{12}H_{10}O_{14}^{-2}$	0.307 0.134 0.152 0.998 1.530	
			Intermediates (I_i)			

***I*$_1$**	2.4	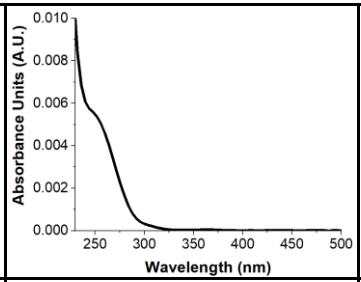	244.939	$Fe^{II}C_6H_5O_7^{-1}$	1.48	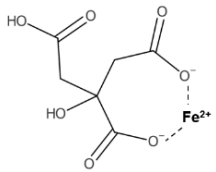 *Iron(II)Citrate based on spectral database match and isotope distribution.*[114]
***I*$_2$**	3.1	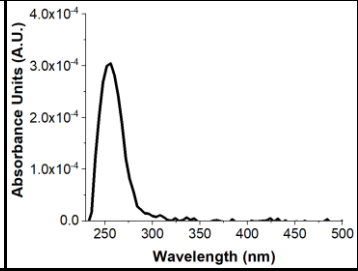	211.028	$Fe^{II}C_5H_{15}O_5^{-1}$	3.2	
			197.012	$Fe^{II}C_4H_{13}O_5^{-1}$	3.2	
***I*$_3$**	6.2	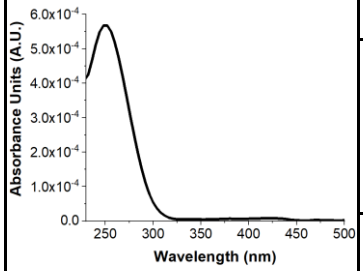	255.018	$Fe^{II}C_6H_{15}O_7^{-1}$	2.01	
			211.028	$Fe^{II}C_5H_{15}O_5^{-1}$	3.2	
			145.014	$C_5H_6O_5$	0.37	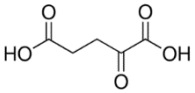 *Alpha-ketoglutaric acid*
***I*$_4$**	8.8		230.923	$Fe^{II}C_5H_3O_7^{-1}$	0.23	
			190.965	$Fe^{II}C_4H_7O_5^{-1}$	0.58	

		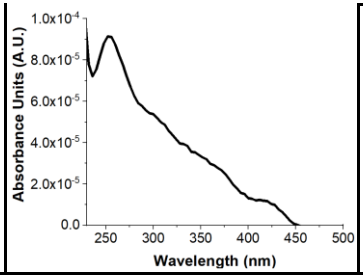	176.949	$Fe^{II}C_3H_5O_5^{-1}$	0.79	
Products (P_i)						
P_1	2.2	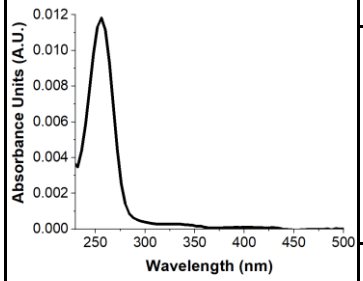	115.004	$C_4H_4O_4$	0.853	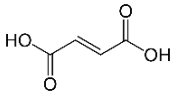 *Fumaric acid*
			147.029	$C_5H_8O_5$	0.200	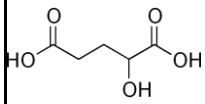 *2-hydroxyglutaric acid*
			261.025	$C_9H_{10}O_9$	0.594	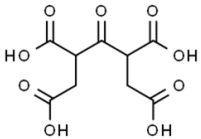 *3-oxo-1,2,4,5-pentanetetracarboxylic acid*
P_2	2.3		231.015	$C_8H_8O_8$	0.431	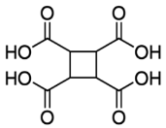 *cyclobutanetetracarboxylic acid*

		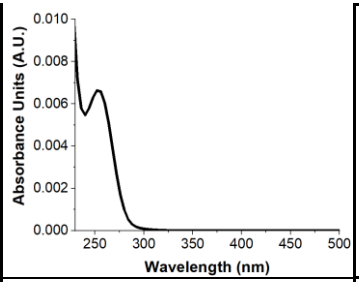	245.030	$C_9H_{10}O_8$	0.451	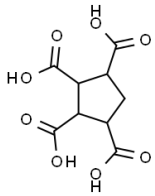 *cyclopentanecarboxylic acid*
***P*$_3$**	2.6	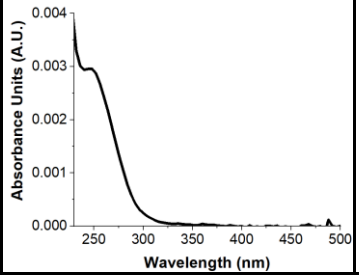	173.009	$C_6H_6O_6$	0.122	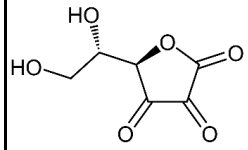 *Dehydroascorbic acid*

491

The identified HPLC-PDA features eluting at RTs of 2.4, 3.1, 6.2, and 8.8 min in the samples from 5 and 40 min irradiation times correspond to Fe^{II}-organic intermediates I_1, I_2, I_3, and I_4, respectively. I_1 is plausibly identified as the reduced mono-charged Fe^{II}-citrate complex, corresponding to $^{56}Fe^{II}C_6H_5O_7^{1-}$, which is chemically different than the Fe^{III}-citrate complex(es) observed as *R* species. Fe^{II}-citrate was detected in all of the photoreacted samples. Extracted ion chromatograms for both $^{56}Fe^{II}Cit$ and $^{56}Fe_2^{III}Cit_2$ complexes eluting at different retention times along with corresponding UV-visible spectra recorded by PDA detector are described in Figure S7 of the SI file. The complexation of Fe^{2+} to citric acid occurs at neutral and alkaline pH conditions (within LC buffer ranges), as the hydroxyl groups in citrate molecule become ionized in solution forming the monomeric Fe^{II}-citrate complex.[115] Our results show that Fe^{II}-citrate and Fe^{III}-citrate are uniquely identifiable and distinguishable in these LC experiments. However, those species are considered unstable and relatively weak complexes in the aqueous solution[116]; therefore it is difficult to quantify Fe^{II}-citrate (aq) in these experiments. Nevertheless, to the best of our knowledge, separated and distinguished Fe^{III}- and Fe^{II}-citrate complexes are shown here for the first time. Detection of these Fe^{II}-citrate intermediates implies that a fraction of these species did not degrade immediately following LMCT conversion of both soluble and oxide bound[108] Fe^{III}-citrate complexes to Fe^{2+} and citrate ions. I_2 corresponds to two coeluting monocharged Fe-organic complexes of $^{56}Fe^{II}C_5H_{15}O_5^{1-}$ and $^{56}Fe^{II}C_4H_{15}O_5^{1-}$ while I_3 corresponds to a mixture of two ions: $^{56}Fe^{II}C_6H_{15}O_7^{1-}$ monocharged complex and α-ketoglutaric di-carboxylic acid ($C_5H_6O_5$), which was reported in a previous study[25] as an abundant organic intermediate in the photodecomposition of Fe^{III}-citrate. Finally, strongly absorbing I_4 feature corresponds to several co-eluting mono-charged ions: $^{56}Fe^{II}C_3H_5O_5^{1-}$, $^{56}Fe^{II}C_4H_7O_5^{1-}$, and $^{56}Fe^{II}C_5H_3O_7^{1-}$, which exhibit maximum absorbance at ~ 250 – 256 nm and tailing in the 350 – 400 nm ranges (see Table 1 and Table S1 of SI file). Consistently with the observed $R \rightarrow I \rightarrow P$ formal kinetics, all *I* features identified here degrade substantially at longer irradiation times and are therefore poorly seen in the 80 and 120 min samples. The degradation of Fe(II) intermediate species here is likely due to the oxidation of Fe^{2+} back to Fe^{3+} in the presence of citrate and available oxygen at the relevant pH conditions similar to previous work.[117] The rate of Fe(II)-citrate oxidation is enhanced in the presence of high concentrations of citrate in the solution,[118] therefore we should expect the rate of Fe(II) oxidation to be proportional to the concentration of citrate ions in the solution.

522 Features *P_1, P_2,* and *P_3,* eluting at 2.2, 2.3, and 2.6 min RT were detected in each of the irradiated
523 mixtures. However, they become most abundant in the 80 and 120 min samples. The plausible
524 identification of *P_1* is a mixture of co-eluting organic compounds such as fumaric acid ($C_4H_4O_4$),
525 2-hydroxyglutaric acid ($C_5H_8O_5$), and 3-oxo-1,2,4,5-pentanetetracarboxylic acid ($C_9H_{10}O_9$), while
526 *P_2* feature is associated with cyclobutanetetracarboxylic ($C_8H_8O_8$) and cyclopentane carboxylic
527 ($C_9H_{10}O_8$) acids. Detection of small organic acid byproducts such as fumaric (C_4) and hydroxy
528 glutaric acid (C_5) in the irradiated mixtures results from decarboxylation of citrate radical in the
529 presence of oxygen (R4 in Scheme 1). In addition, plausible Norrish I and II photodegradation
530 pathways (R10-11 in Scheme 1) are the source of small organic acids with C=C double bonds and
531 other radical recombinant species (R-R). Photolysis of citric acid by $OH^{\bullet}$ mediated heterogenous
532 oxidation in a separate study[119] results in extensive fragmentation of C-C bonds through acid-base,
533 free-radical chemical reactions, as well as decarboxylation and formation of carboxyl and
534 carbonyl-groups. Therefore, fumaric acid, 2-hydroxy glutaric acid and other small molecules are
535 expected byproducts of the decarboxylation and they are also common enzymatic metabolites in
536 the citric acid 'Krebs' cycle.[120] Alternatively, detection of highly oxygenated multi-carboxylic
537 acid and hydroxy dimers in this photolyzed system, such as $C_7H_8O_8$, $C_8H_{10}O_9$, and $C_{10}H_{12}O_{10}$, are
538 consistent with a previous study investigating the heterogenous photooxidation of dicarboxylic
539 acids catalyzed on the surface of TiO_2/Fe_2O_3 dust particles.[121] Carboxylic dimer products can arise
540 from radical-radical recombination reactions (R9-10 in Scheme 1) of two carboxylic monomer
541 radicals in the irradiated solution. Lastly, HPLC feature *P_3* eluting at 2.6 min RT corresponds
542 plausibly to dehydroascorbic acid ($C_6H_6O_6$), a cyclic molecule with multiple carbonyl (C=O)
543 groups and two hydroxyl groups. The characteristic absorption profile of this molecule is similar
544 to that reported in previous study[122] investigating similar species and ascorbic acid via HPLC-
545 PDA. However, this molecule may also undergo consequent Norrish photochemistry or
546 reactions[123] with H_2O_2 to yield other oxidized, ring-opening products such as $C_6H_8O_8$ detected in
547 the irradiated samples. Full list of identified CHO-containing species is included in Table S3 of
548 the SI file. Overall, cyclic Fe redox reactions in the solution catalyzes the oxidation of citrate to
549 several of the intermediate and product species representing structurally similar species.

550

Optical Properties of the Irradiated Samples Figure 3 illustrates contributions of individual *R, I* and *P* components to $MAC(\lambda)_{\Sigma}^{PDA}$ spectra recorded by HPLC-PDA for each of the five analyzed samples. Overall, the systematic and quantitative changes in the absolute values of $MAC(\lambda)_{\Sigma}^{PDA}$ and the relative fractions of *R, I* and *P* contributions can be observed as the photolysis reactions progress. Components *R* dominate absorbance in the unreacted sample. Their contribution is halved in the sample irradiated for 5 min, where contributions by the *R* and *I* components become nearly equal, and influence of the *P* components also becomes detectable. At the later irradiation times (40 – 120 min), contributions from *P* continue to grow, while contributions from *I* decline and contributions from *R* are undetectable. Notably, absolute values of $MAC(\lambda)_{\Sigma}^{PDA}$ decline steadily as the photolysis reactions proceed and the spectral shape changes from featureless to more defined with a well-distinguished peak at 256 nm. At 80 – 120 min irradiation time, the $MAC(\lambda)_{\Sigma}^{PDA}$ values decrease by a factor of ~5 compared to those measured for the unreacted sample. These observations are in striking contrast to the $MAC(\lambda)_{bulk}$ measurements using a UV-vis spectrophotometer shown in Figures 1a and 1b. While both measurements show the same trend of the *MAC* declining during the photolysis, absorption detected by the UV-vis spectroscopy of bulk samples is much higher than that inferred from the HPLC-PDA measurements of the same samples. The plausible reason for this discrepancy is a difference in the analyte material probed in two measurements. Specifically, the $MAC(\lambda)_{bulk}$ spectra reflect absorption by total organic carbon (TOC) which includes dissolved water-soluble organic carbon (WSOC) and colloids, while the $MAC(\lambda)_{\Sigma}^{PDA}$ spectra correspond to the light absorption by WSOC only. Therefore $MAC(\lambda)_{\Sigma}^{PDA} \stackrel{\text{def}}{=} MAC(\lambda)_{\Sigma}^{WSOC}$.

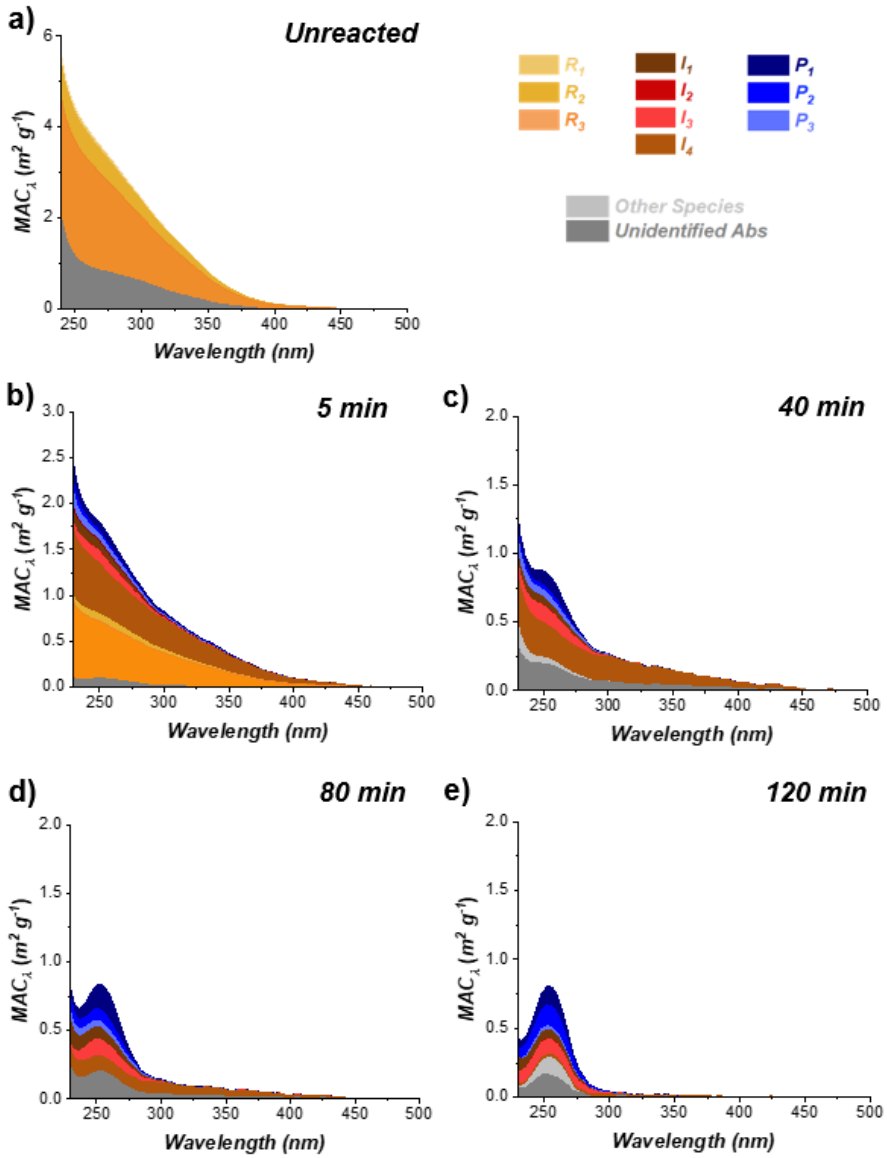

Figure 3: Fractions of $MAC(\lambda)_{\Sigma}^{PDA}$ attributed to water-soluble individual components of the Fe^{III}-citrate irradiated mixtures. Orange, brown, and blue colors indicate contributions from reactants (*R*), intermediates (*I*), and products (*P*) defined in Figure 2.

Figure 4 further illustrates the relationship between $MAC(\lambda)_{bulk}$ and $MAC(\lambda)_{\Sigma}^{WSOC}$ values determined for all 5 samples studied here. Individual panels illustrate relative fractions of $MAC(\lambda)_{\Sigma}^{WSOC}$ and $MAC(\lambda)_{colloids}$ out of $MAC(\lambda)_{bulk}$ spectra measured for the unreacted and irradiated samples. The $MAC(\lambda)_{\Sigma}^{WSOC}$ is the major fraction of $MAC(\lambda)_{bulk}$ for the unreacted and 5 min irradiated mixtures, suggesting only minor effects of colloids (likely $Fe(OH)_3$) at the beginning of reaction. At later irradiation times (40-120 min), the buildup of colloidal products is

evident from increased values of $MAC(\lambda)_{colloids} = MAC(\lambda)_{bulk} - MAC(\lambda)_{\Sigma}^{WSOC}$ illustrated in the plots. The $MAC(\lambda)_{colloids}$ absorbing fraction in these mixtures is presumably related to formation of insoluble $Fe(OH)_3$ and poorly soluble reduced carbon products of reactions R12 (Scheme 1) that contribute to formation and growth of colloids. To test this assumption, we conducted a focused study to provide insights on the sizes, concentration, and chemical composition of these colloidal products.

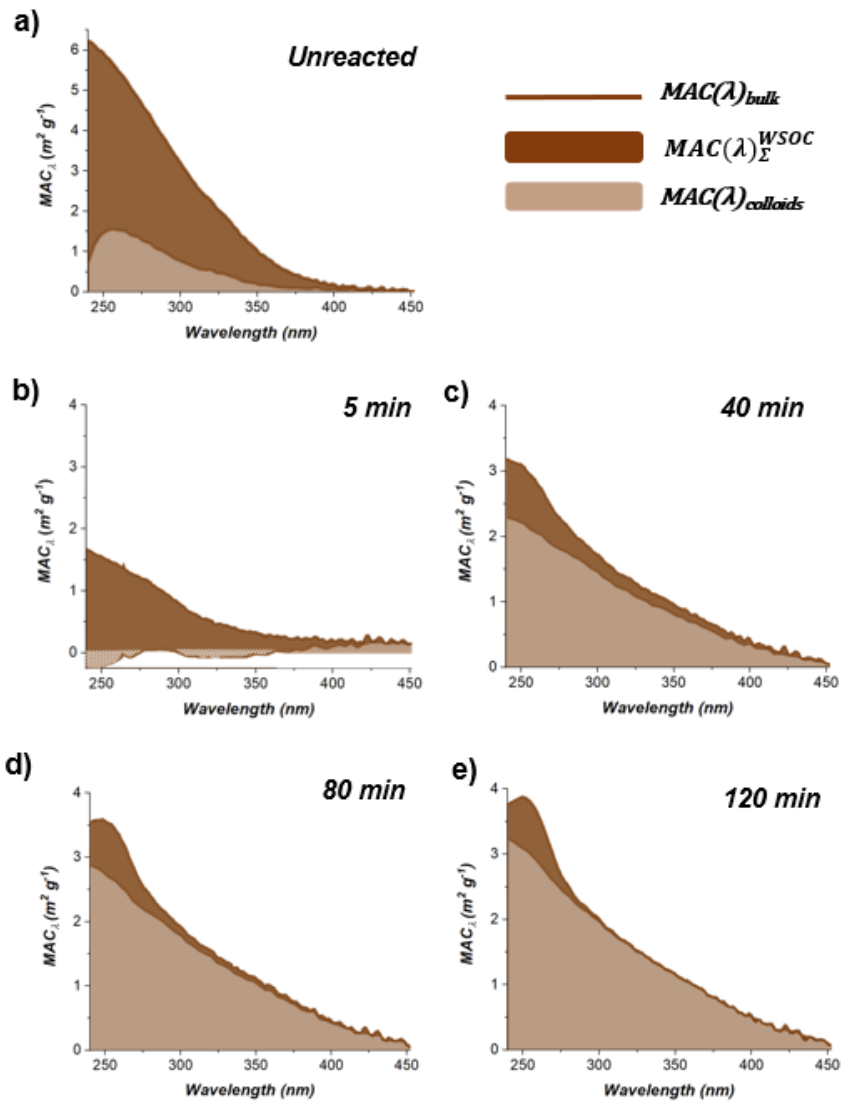

Figure 4. The relative fractions of $MAC(\lambda)_{\Sigma}^{WSOC}$ and $MAC(\lambda)_{colloids}$ out of $MAC(\lambda)_{bulk}$ spectra measured for the samples analyzed in this study.

***In Situ* Flow Microscopy Detection of Colloids** Colloidal components of the unreacted and irradiated samples at 5, 40, 80, and 120 min were measured using the FlowCam® Nano oil immersion flow microscope that is capable to image and count individual colloidal particles larger than 0.3 mm. Figures 5a-5e shows the 8-bin per decade number size distributions ($\Delta N/\Delta \log D_p$; particles cm^{-3}) for the unreacted, 5 min, 40, 80 min, and 120 min photoreacted samples. In the unreacted sample, the particle number concentration is low. The representative particle images (included in Figure S8 of the SI file) reveal relatively smaller and round colloidal particles in the unreacted system, which are likely commonly occurring $Fe(OH)_3$ colloids and the presumed oxide bound Fe^{III}-citrate particles. As the photolysis progresses from 5 – 120 min, the number concentrations and size distributions of the particles detected grow in the reacted solutions, which reveal significantly larger and more fractional colloids, as shown in Figure S8 of the SI file. The estimated mass loadings shown in Figure 5f indicate progressive increase from <50 μg/L in the unreacted sample to >1000 μg/L in the irradiated samples. Ranges of lower and upper mass limits are shown to reduce bias of larger particles (> 3 μm) that are sparsely present. Details of the data analysis are described in Appendix F of the SI file. With respect to the unreacted sample, the mass-size distributions are shifted to larger particle sizes, suggesting that reduced carbon components formed after prolonged photolysis contribute to the buildup of colloids in the irradiated samples (see Figure S9 of the SI file). The mass loading of colloids in the 80 and 120 min irradiated sample corresponds to ~ 8% and 5% of the original Fe(III)-Cit reactant mass. However, particles within the 0.3 – 0.5 μm size ranges contribute most to the observed scattering of UV-visible light in the near visible regions of the absorption spectrum shown in Figure 1a. Nevertheless, these results show the formation of new colloids that effectively increase in concentration under prolonged irradiation to UV-Vis light, representing an important pathway to nanoparticle products formation in photochemical Fe^{III}-carboxylate systems.

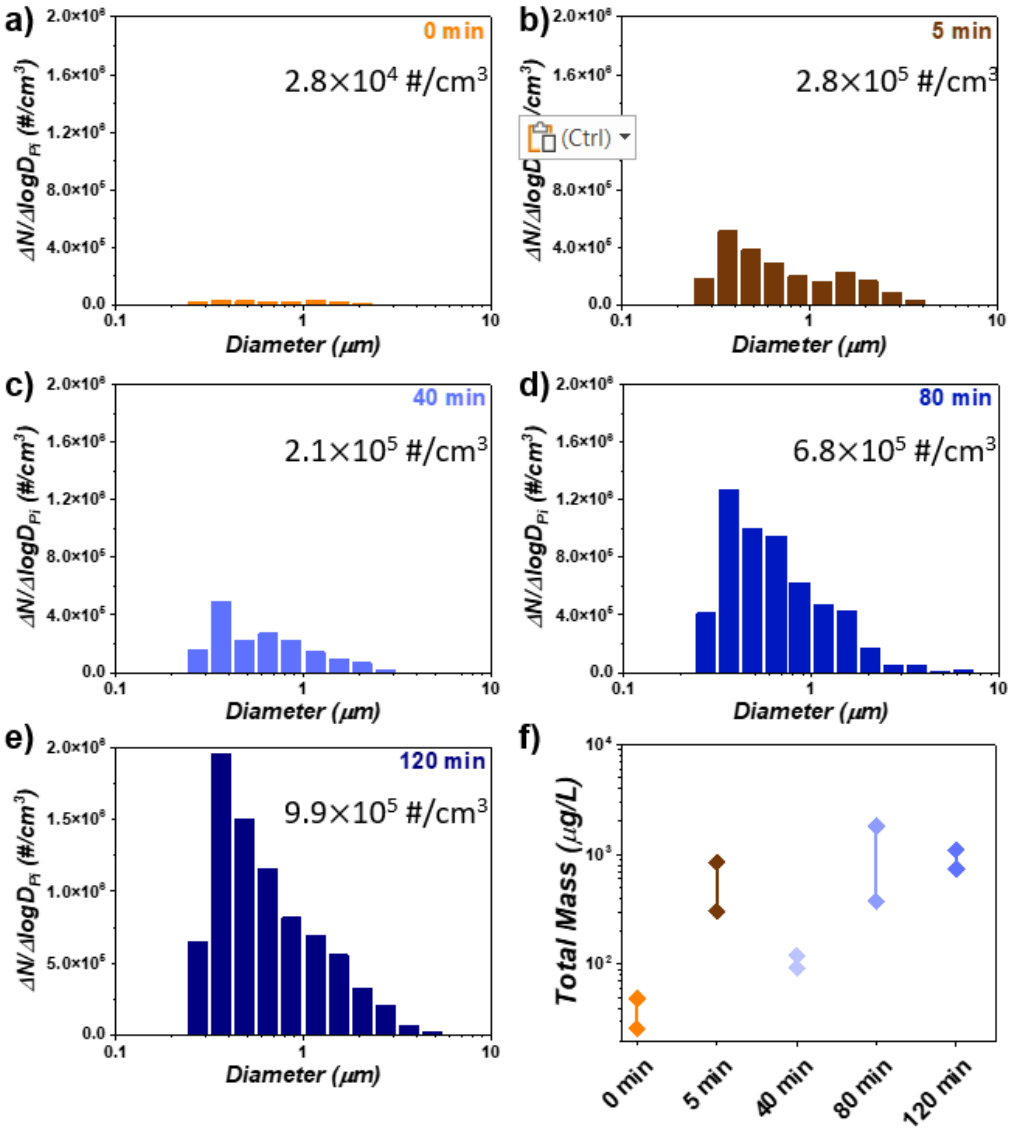

Figure 5. Particle number size distribution of colloids detected in the unreacted (orange) and photoreacted samples at 5 (brown), 40, 80, and 120 min (light blue - dark blue). Diameter reported by the flow microscope is the equivalent size diameter (ESD) in µm. Calculated mass loadings for each of the cases are reported as upper and lower limit values in panel f (see Fig S9 for additional details).

Chemical Characterization of Colloidal Material Colloidal material found in the 120 min irradiated sample was used for chemical characterization. Extracted colloidal material was dissolved in the '*org-mix*' solvent and the obtained solutions were analyzed in DI-ESI(+)-HRMS

experiments for detection of high molecular weight components formed from radical recombination (R12 of Scheme 1). Figure 6a illustrates results of the ESI(+)-HRMS analysis, indicating MS features identified and assigned in the 500-1100 Da mass range. The representative inset plot in Figure 6a illustrates selected CHO peaks and their formula assignments in the 650-730 m/z range. Figure 6b and 6c show the hydrogen-to-carbon (H/C) elemental ratios and DBE of species found in colloidal components, plotted as a function of number of carbon atoms (C) and color-coded by their oxygen-to-carbon (O/C) ratio (Figure 6b). Reference lines in Figure 6c correspond to cata-PAH′s (DBE = 0.75 × C − 0.5)[124] and linear conjugated polyenes C_xH_x+2 (DBE = 0.5 × C).[125] The molecular species representative of dissolved colloids in this HRMS dataset span 30 – 60 carbon atoms with varying degree of oxygenation and unsaturation due to double bonds in the organic structures. The adsorbed components of the colloidal material is composed of moderately saturated aliphatic and unsaturated hydrocarbon species with variable DBE and low oxygen content. Majority of the assigned features with higher HRMS signal intensity fall below the linear conjugated polyene boundary line, while some of the lower intensity features fall closer to the condensed aromatic reference line. Few selected species such as: $C_{34}H_{64}O_{11}$ (DBE = 3; O/C = 0.32), $C_{37}H_{56}O_{12}$ (DBE = 10; O/C = 0.32), $C_{40}H_{62}O_8$ (DBE = 10; O/C = 0.2), $C_{47}H_{58}O_5$ (DBE = 19; O/C = 0.11), and $C_{49}H_{54}O_5$ (DBE = 23; O/C = 0.1) represent less oxygenated/ more reduced carbon fragments that were adsorbed on colloid surfaces.

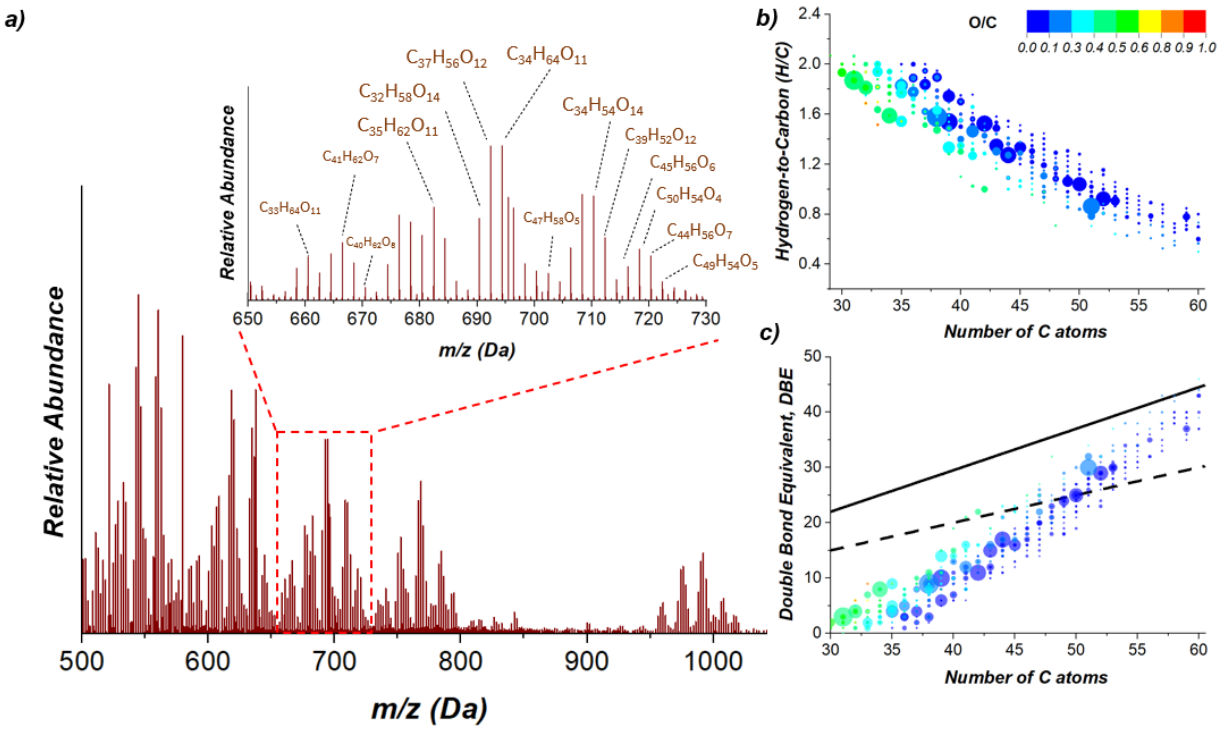

Figure 6. a) (+)ESI-HRMS spectrum representative of the '*org-mix'* digested colloidal components identified in the Fe^{III}-citrate mixture irradiated for 120 min. Inset plot shows zoomed in HRMS spectrum in the range 650-730 Da, b) H/C ratio vs number of carbon atoms (C) plot and c) DBE vs C plot scaled to O/C ratio. Reference lines represent DBE values of linear polyenes (dotted line; 0.5×C)[125] and condensed aromatics (dashed line; 0.75×C-0.5).[124] The size of all individual symbols is scaled to the square root of the MS peak intensity.

Overall, we observe unique low and high molecular weight features in the mixture compromising dissolved colloid fragments composed of *C*, *H* and *O* immediately following dissolution in *'org-mix'* followed by ultrasonication. Of note, those features were only observed in the HRMS spectra of sonicated samples, confirming their apportionment to the degraded colloids (see Figure S9 of SI file for more details). Furthermore, those features were also absent in MS spectra acquired from the unreacted sample prepared following the same dissolution procedures (see Figure S10 of the SI file). Therefore, adsorbed colloidal analytes probed at the longer photolysis time are composed of less oxygenated (more reduced) carbon material, resulting from the radical recombination reactions in R12 of Scheme 1.

CONCLUSIONS

This study investigated multi-phase photochemistry of Fe-citrate and reported on the formation of unexplored colloidal products under prolonged light exposure. Apparent reaction rates of the $R \xrightarrow{j_1} I \xrightarrow{j_2} P$ formal kinetics derived from our experiments are $j_1 \sim 0.12$ min^{-1} and $j_2 \sim 0.05$ min^{-1}, which correspond to the laboratory half-lifetimes of $\tau_{lab} \sim 8.3$ and 20 min, respectively (Appendix D). Scaling these half -lifetimes with respect to intensity of the solar radiation at summer solstice in Southern California and Mediterranean region suggests environmental half-lifetimes of ~ 32 min and ~1.3 hr, respectively. (Appendixes G and H). Therefore, we conclude that photochemical formation of colloidal products with carbon in a relatively reduced oxidation state may take place at the time scale relevant to the real-world environment of the Fe-carboxylate systems.

The light-absorbing properties of the photochemically reacting Fe-citrate mixtures are very much dynamic and overall comparable to those reported for atmospheric brown carbon (BrC). Figure 7 illustrates the $MAC(\lambda)_{bulk}$ values for the Fe-citrate samples of our study shown with respect to the optical-based AAE versus $MAC_{405\text{nm}}$ classification framework.[70,95,126,127] The light-absorbing properties of the unreacted and photoreacted Fe-citrate mixtures are skewed between weak (W) and moderate (M) light-absorbing classes, and they are less-absorbing than BrC from biomass burning [93,128] Over the course photochemical aging, BrC characteristics of the Fe-citrate mixture follows the $W \rightarrow M$ transition, resulting in stronger absorption by the photoreacted mixtures. This darkening is largely attributed to the carbonaceous colloidal material formed after prolonged photolysis under oxygen-deprived conditions. To date, no study has observed these systematic changes of Fe^{III}-carboxylates leading to production of insoluble carbonaceous colloids in aqueous photochemical reactions. To that extent, we therefore presume that formation of condensed reduced carbon species in this system is most likely similar to other extensively photolyzed brown carbon proxies,[129] and other Fe^{III}-carboxylate systems.[20,24,34]

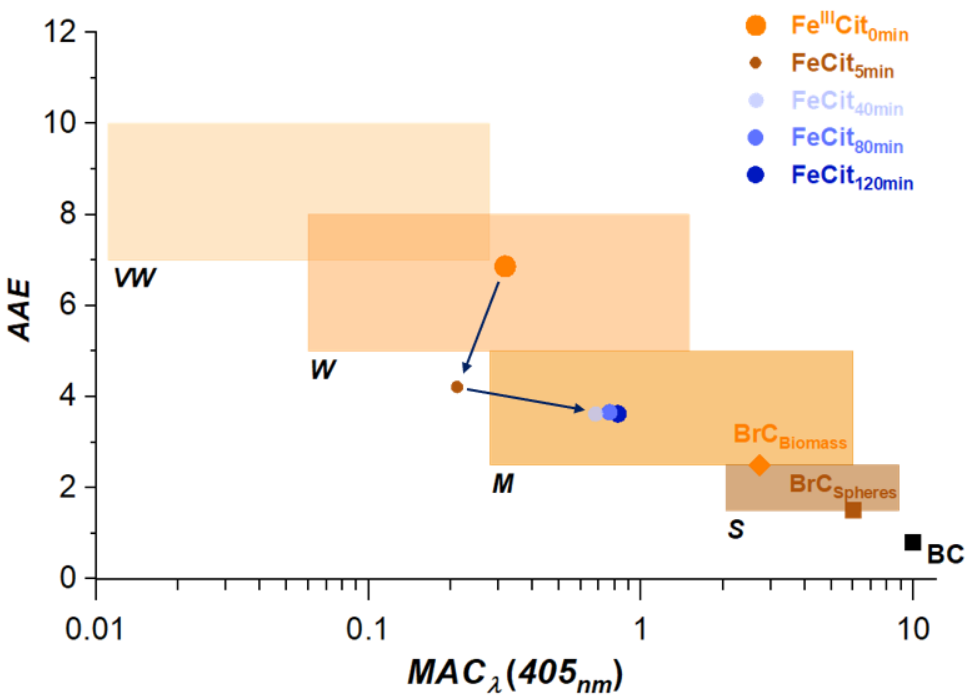

Figure 7. Optical properties of Fe-citrate photolysis samples mapped in the *AAE-MAC*$_{405\ nm}$ space introduced by *Saleh*.[126] The shaded regions represent "optical bins" for "very weak (VW)", "weak (W)", "moderate (M)", and "strong (S)" absorbing BrC classes. Literature-reported *MAC* values at 405 nm for BrC related to biomass burning,[93] spherical tar-balls,[128] and black carbon (BC)[130] are shown.

Overall, the results of this work demonstrate a multi-phase mechanism of the Fe^{III}-citrate photochemistry in aquatic systems of environmental relevance. The photochemical products identified in this representative Fe^{III}-carboxylate system are water-soluble components (*R*, *I*, and *P* components) and carbonaceous colloids formed under oxygen-deprived conditions in the extensively photolyzed mixtures. The detection of colloidal products in this system may contribute to yet unrecognized atmospheric and terrestrial light-absorbing material in aquatic environments with direct effects on the radiative forcing of climate. Further investigation of additional photoreactive Fe^{III}-carboxylate systems need to consider and account for formation of colloidal products that remain poorly characterized, overlooked in previous studies, and received little attention in the literature.[62,131] In particular, ferric oxalate in natural aquatic environments may also behave similarly in the context of our work. Aqueous photolysis of ferric oxalate complex as shown in Figure S11 of the SI file follows similar trend, where degradation of Fe(III)-oxalate complex occurs, followed by formation of short-lived Fe(II)-intermediate species, and build-up of

704 water-soluble and insoluble colloidal reaction products where the light extinction extends beyond
705 500nm. Additionally, the aqueous photolysis of Fe-carboxylate complexes in natural waters are
706 important for $Fe^{III/II}$ catalytic cycling, controlling the bioavailability of Fe(II) to microorganisms,[132]
707 photo-mineralization of DOM, and oxidation of organic carbon in irradiated environmental waters
708 and in atmospheric aerosol particles.[62,133–135]

709 Photoreactive Fe-carboxylates may also play an important role in initiating photocatalytic
710 reactions in snowpack. In particular, snow covered areas of inland central Asia[127,136–138] located
711 near Fe^{III} dust sources may serve as an important medium for photocatalytic cycling of Fe^{III}-
712 carboxylates and the subsequent photooxidation of other water-soluble species (i.e. brown carbon,
713 carboxylic acids, ketones), halogenated species, and other inorganics in the snowpack. The
714 interactions of externally mixed Fe-mineral dust[137] and subsequent photochemical transformations
715 due to Fe^{III}-carboxylates can significantly enhance light absorption and modify the resulting snow
716 and surface albedo, with implications to indirect radiative forcing changes on the snow/surface
717 energy budgets. Specifically, carbonaceous colloid products resulted from Fe-carboxylate
718 photochemistry may accelerate melting of the snowpack, similar to BC and BrC deposits,[136]
719 leading to reduction of the snow albedo.

720

721 SUPPORTING INFORMATION

722 Appendix A and Figure S1 describe transient optical and photochemical experimental setup of this
723 study; Appendix B and Figure S2 describes chemical actinometry experiments and relevant
724 calculations; Appendix C describes detailed direct infusion-HRMS parameters; Appendix D, E, F,
725 G, and H describes the formal kinetic modelling, quantum yields, particle size distributions,
726 atmospheric scaling, and TUV model calculations and selected parameters, respectively. Figure
727 S3 illustrates experimental quantitation of dissolved Fe^{2+} and calibration curve of Fe^{II}-
728 phenanthroline complexes; Figure S4 illustrate selected ion chromatograms (SIC`s) of Fe^{III}-citrate
729 complex ions; Figure S5 and S6 describe DI-HRMS screening and MS^2 experiments of Fe^{III}-citrate
730 complexes for identification and structural characterization. Figure S7 illustrates SIC`s for $Fe^{III/II}$-
731 citrate complexes detected in HPLC-HRMS. Figure S8 show *in situ* FlowCam Nano images of
732 colloidal particles. Figure S9 shows mass size distributions of colloids detected by FlowCam Nano.

Figure S10, S11 illustrate DI-HRMS results of dissolved colloidal products under specified conditions. Figure S12 UV-visible spectrum of ferric oxalate photolysis. List of all molecular assignments in HPLC-PDA-HRMS and DI-HRMS are reported in Table S1, S2, and S3.

Data Availability The dataset used for this work is available for download as a .zip file from https://doi.org/10.4231/xxx-yyyy (West et al., 2022).

AUTHOR INFORMATION

Corresponding Author

Alexander Laskin − Department of Chemistry, Purdue University, Indiana 47906, United States; orcid.org/0000- 0002-7836-8417; Email: alaskin@purdue.edu

Authors

Christopher P. West − Department of Chemistry, Purdue University, Indiana 47906, United States; orcid.org/0000- 0001-9337-2820

Jackson T. Ryan − Department of Chemistry, Purdue University, Indiana 47906, United States

Ana C. Morales − Department of Chemistry, Purdue University, Indiana 47906, United States; orcid.org/0000-0001-6969-2883

Maria V. Misovich − Department of Chemistry, Purdue University, Indiana 47906, United States; orcid.org/0000-0001-6748-049X

Anusha P. S. Hettiyadura − Department of Chemistry, Purdue University, Indiana 47906, United States; orcid.org/0000-0002-5757-9784

Felipe Rivera-Adorno − Department of Chemistry, Purdue University, Indiana 47906, United States; orcid.org/0000-0002-7355-7999

Jay M. Tomlin − Department of Chemistry, Purdue University, Indiana 47906, United States; orcid.org/0000-0002-3081-1512

Andrew Darmody − Department of Chemistry, Purdue University, Indiana 47906, United States; orcid.org/0000- 0002-7749-397X

Brittany N. Linn − Department of Chemistry, Purdue University, Indiana 47906, United States

Peng Lin − Department of Chemistry, Purdue University, Indiana 47906, United States

Author Contributions. C.P.W and A.L designed the overall project framework and experiments. C.P.W, J.R, M.M, and B.N.L performed the photolysis and chemical actinometry experiments. C.P.W, M.M, A.P.S.H, and P.L performed the LC separations and method development protocols. C.P.W performed the molecular characterization experiments and processed, analyzed, and interpreted the hyphenated LC-PDA-HRMS and direct infusion HRMS data with the assistance of J.R, A.D., and B.N.L. F.R and J.M.T performed microscopy imaging. C.P.W and A.C.M performed FlowCam measurements and data analysis. A.C.M designed custom MATLAB scripts used for processing and analysis of all UV-visible spectroscopy data in this work. C.P.W and A.L wrote the manuscript with contributions with all co-authors.

Competing Interests. The authors declare that they have no conflict of interest.

Acknowledgments. We acknowledge support from the startup funds allocated to A. Laskin by the Department of Chemistry at Purdue University and partial support from the National Science Foundation award AGS-2039985 at the time of this manuscript preparation.

REFERENCES

(1) Huang, J.; Jones, A.; Waite, T. D.; Chen, Y.; Huang, X.; Rosso, K. M.; Kappler, A.; Mansor, M.; Tratnyek, P. G.; Zhang, H. Fe(II) Redox Chemistry in the Environment. *Chem. Rev.* **2021**. https://doi.org/10.1021/acs.chemrev.0c01286.

(2) Taylor, K. G.; Konhauser, K. O. Iron in Earth Surface Systems: A Major Player in Chemical and Biological Processes. *Elements* **2011**, *7* (2), 83–88. https://doi.org/10.2113/gselements.7.2.83.

(3) Taylor, S. R. Abundance of Chemical Elements in the Continental Crust: A New Table. *Geochim. Cosmochim. Acta* **1964**, *28* (8), 1273–1285. https://doi.org/10.1016/0016-7037(64)90129-2.

(4) Hutchins, D. A.; Boyd, P. W. Marine Phytoplankton and the Changing Ocean Iron Cycle. *Nat. Clim. Change* **2016**, *6* (12), 1072–1079. https://doi.org/10.1038/nclimate3147.

(5) Lis, H.; Shaked, Y.; Kranzler, C.; Keren, N.; Morel, F. M. M. Iron Bioavailability to Phytoplankton: An Empirical Approach. *ISME J.* **2015**, *9* (4), 1003–1013. https://doi.org/10.1038/ismej.2014.199.

(6) Boyd, P. W.; Jickells, T.; Law, C. S.; Blain, S.; Boyle, E. A.; Buesseler, K. O.; Coale, K. H.; Cullen, J. J.; Baar, H. J. W. de; Follows, M.; Harvey, M.; Lancelot, C.; Levasseur, M.; Owens, N. P. J.; Pollard, R.; Rivkin, R. B.; Sarmiento, J.; Schoemann, V.; Smetacek, V.; Takeda, S.; Tsuda, A.; Turner, S.; Watson, A. J. Mesoscale Iron Enrichment Experiments 1993-2005: Synthesis and Future Directions. *Science* **2007**, *315* (5812), 612–617. https://doi.org/10.1126/science.1131669.

(7) Jickells, T. D.; An, Z. S.; Andersen, K. K.; Baker, A. R.; Bergametti, G.; Brooks, N.; Cao, J. J.; Boyd, P. W.; Duce, R. A.; Hunter, K. A.; Kawahata, H.; Kubilay, N.; laRoche, J.; Liss, P. S.; Mahowald, N.; Prospero, J. M.; Ridgwell, A. J.; Tegen, I.; Torres, R. Global Iron Connections Between Desert Dust, Ocean Biogeochemistry, and Climate. *Science* **2005**, *308* (5718), 67–71. https://doi.org/10.1126/science.1105959.

(8) Sedwick, P. N.; Sholkovitz, E. R.; Church, T. M. Impact of Anthropogenic Combustion Emissions on the Fractional Solubility of Aerosol Iron: Evidence from the Sargasso Sea. *Geochem. Geophys. Geosystems* **2007**, *8* (10). https://doi.org/10.1029/2007GC001586.

(9) Gonet, T.; Maher, B. A. Airborne, Vehicle-Derived Fe-Bearing Nanoparticles in the Urban Environment: A Review. *Environ. Sci. Technol.* **2019**, *53* (17), 9970–9991. https://doi.org/10.1021/acs.est.9b01505.

(10) Deguillaume, L.; Leriche, M.; Desboeufs, K.; Mailhot, G.; George, C.; Chaumerliac, N. Transition Metals in Atmospheric Liquid Phases: Sources, Reactivity, and Sensitive Parameters. *Chem. Rev.* **2005**, *105* (9), 3388–3431. https://doi.org/10.1021/cr040649c.

(11) Tomlin, J. M.; Jankowski, K. A.; Rivera-Adorno, F. A.; Fraund, M.; China, S.; Stirm, B. H.; Kaeser, R.; Eakins, G. S.; Moffet, R. C.; Shepson, P. B.; Laskin, A. Chemical Imaging of Fine Mode Atmospheric Particles Collected from a Research Aircraft over Agricultural Fields. *ACS Earth Space Chem.* **2020**, *4* (11), 2171–2184. https://doi.org/10.1021/acsearthspacechem.0c00172.

(12) Cwiertny, D. M.; Baltrusaitis, J.; Hunter, G. J.; Laskin, A.; Scherer, M. M.; Grassian, V. H. Characterization and Acid-Mobilization Study of Iron-Containing Mineral Dust Source Materials. *J. Geophys. Res. Atmospheres* **2008**, *113* (D5). https://doi.org/10.1029/2007JD009332.

(13) Al-Abadleh, H. A. Aging of Atmospheric Aerosols and the Role of Iron in Catalyzing Brown Carbon Formation. *Environ. Sci. Atmospheres* **2021**, *1* (6), 297–345. https://doi.org/10.1039/D1EA00038A.

(14) Tagliabue, A.; Bowie, A. R.; Boyd, P. W.; Buck, K. N.; Johnson, K. S.; Saito, M. A. The Integral Role of Iron in Ocean Biogeochemistry. *Nature* **2017**, *543* (7643), 51–59. https://doi.org/10.1038/nature21058.

(15) Kappler, A.; Bryce, C.; Mansor, M.; Lueder, U.; Byrne, J. M.; Swanner, E. D. An Evolving View on Biogeochemical Cycling of Iron. *Nat. Rev. Microbiol.* **2021**, *19* (6), 360–374. https://doi.org/10.1038/s41579-020-00502-7.

(16) Lovley, D. R.; Holmes, D. E.; Nevin, K. P. Dissimilatory Fe(III) and Mn(IV) Reduction. In *Advances in Microbial Physiology*; Academic Press, 2004; Vol. 49, pp 219–286. https://doi.org/10.1016/S0065-2911(04)49005-5.

(17) Bosch, J.; Heister, K.; Hofmann, T.; Meckenstock, R. U. Nanosized Iron Oxide Colloids Strongly Enhance Microbial Iron Reduction. *Appl. Environ. Microbiol.* **2010**, *76* (1), 184–189. https://doi.org/10.1128/AEM.00417-09.

(18) Roden, E. E. Geochemical and Microbiological Controls on Dissimilatory Iron Reduction. *Comptes Rendus Geosci.* **2006**, *338* (6), 456–467. https://doi.org/10.1016/j.crte.2006.04.009.

(19) Lueder, U.; Barker Jørgensen, B.; Kappler, A.; Schmidt, C. Photochemistry of Iron in Aquatic Environments. *Environ. Sci. Process. Impacts* **2020**, *22* (1), 12–24. https://doi.org/10.1039/C9EM00415G.

(20) Pozdnyakov, I. P.; Kolomeets, A. V.; Plyusnin, V. F.; Melnikov, A. A.; Kompanets, V. O.; Chekalin, S. V.; Tkachenko, N.; Lemmetyinen, H. Photophysics of Fe(III)–Tartrate and Fe(III)–Citrate Complexes in Aqueous Solutions. *Chem. Phys. Lett.* **2012**, *530*, 45–48. https://doi.org/10.1016/j.cplett.2012.01.051.

(21) Vukosav, P.; Mlakar, M.; Tomišić, V. Revision of Iron(III)–Citrate Speciation in Aqueous Solution. Voltammetric and Spectrophotometric Studies. *Anal. Chim. Acta* **2012**, *745*, 85–91. https://doi.org/10.1016/j.aca.2012.07.036.

(22) Weller, C.; Horn, S.; Herrmann, H. Photolysis of Fe(III) Carboxylato Complexes: Fe(II) Quantum Yields and Reaction Mechanisms. *J. Photochem. Photobiol. Chem.* **2013**, *268*, 24–36. https://doi.org/10.1016/j.jphotochem.2013.06.022.

(23) Pozdnyakov, I. P.; Melnikov, A. A.; Tkachenko, N.; Chekalin, S. V.; Lemmetyinen, H.; Plyusnin, V. F. Ultrafast Photophysical Processes for Fe(III)-Carboxylates. *Dalton Trans.* **2014**, *43* (47), 17590–17595. https://doi.org/10.1039/C4DT01419G.

(24) Glebov, E. M.; Pozdnyakov, I. P.; Grivin, V. P.; Plyusnin, V. F.; Zhang, X.; Wu, F.; Deng, N. Intermediates in Photochemistry of Fe(III) Complexes with Carboxylic Acids in Aqueous Solutions. *Photochem. Photobiol. Sci.* **2011**, *10* (3), 425–430. https://doi.org/10.1039/C0PP00151A.

(25) Abrahamson, H. B.; Rezvani, A. B.; Brushmiller, J. G. Photochemical and Spectroscopic Studies of Complexes, of Iron(III) with Citric Acid and Other Carboxylic Acids. *Inorganica Chim. Acta* **1994**, *226* (1), 117–127. https://doi.org/10.1016/0020-1693(94)04077-X.

(26) Weller, C.; Tilgner, A.; Bräuer, P.; Herrmann, H. Modeling the Impact of Iron–Carboxylate Photochemistry on Radical Budget and Carboxylate Degradation in Cloud Droplets and Particles. *Environ. Sci. Technol.* **2014**, *48* (10), 5652–5659. https://doi.org/10.1021/es4056643.

(27) George, C.; D'Anna, B.; Herrmann, H.; Weller, C.; Vaida, V.; Donaldson, D. J.; Bartels-Rausch, T.; Ammann, M. Emerging Areas in Atmospheric Photochemistry. In *Atmospheric and Aerosol Chemistry*; McNeill, V. F., Ariya, P. A., Eds.; Topics in Current Chemistry; Springer: Berlin, Heidelberg, 2014; pp 1–53. https://doi.org/10.1007/128_2012_393.

(28) Mangiante, David. M.; Schaller, R. D.; Zarzycki, P.; Banfield, J. F.; Gilbert, B. Mechanism of Ferric Oxalate Photolysis. *ACS Earth Space Chem.* **2017**, *1* (5), 270–276. https://doi.org/10.1021/acsearthspacechem.7b00026.

(29) Borer, P.; Hug, S. J. Photo-Redox Reactions of Dicarboxylates and α-Hydroxydicarboxylates at the Surface of Fe(III)(Hydr)Oxides Followed with in Situ ATR-FTIR Spectroscopy. *J. Colloid Interface Sci.* **2014**, *416*, 44–53. https://doi.org/10.1016/j.jcis.2013.10.030.

(30) Herrmann, H.; Schaefer, T.; Tilgner, A.; Styler, S. A.; Weller, C.; Teich, M.; Otto, T. Tropospheric Aqueous-Phase Chemistry: Kinetics, Mechanisms, and Its Coupling to a Changing Gas Phase. *Chem. Rev.* **2015**, *115* (10), 4259–4334. https://doi.org/10.1021/cr500447k.

(31) Wasgestian, F. V. Balzani Und V. Carassiti: Photochemistry of Coordination Compounds. Academic Press, London, New York 1970. 432 Seiten. Preis: 150 s.; 1971. https://doi.org/10.1002/BBPC.19710750220.
(32) Cieśla, P.; Kocot, P.; Mytych, P.; Stasicka, Z. Homogeneous Photocatalysis by Transition Metal Complexes in the Environment. *J. Mol. Catal. Chem.* **2004**, *224* (1), 17–33. https://doi.org/10.1016/j.molcata.2004.08.043.
(33) Feng, W.; Nansheng, D.; Glebov, E. M.; Pozdnyakov, I. P.; Grivin, V. P.; Plyusnin, V. F.; Bazhin, N. M. Kinetics and Mechanism of Photolysis of the Iron(III) Complex with Tartaric Acid. *Russ. Chem. Bull.* **2007**, *56* (5), 900–903. https://doi.org/10.1007/s11172-007-0136-7.
(34) Pozdnyakov, I. P.; Kel, O. V.; Plyusnin, V. F.; Grivin, V. P.; Bazhin, N. M. New Insight into Photochemistry of Ferrioxalate. *J. Phys. Chem. A* **2008**, *112* (36), 8316–8322. https://doi.org/10.1021/jp8040583.
(35) Zhang, X.; Gong, Y.; Wu, F.; Deng, N.; Pozdnyakov, I. P.; Glebov, E. M.; Grivin, V. P.; Plyusnin, V. F.; Bazhinb, N. M. Photochemistry of the Iron(III) Complex with Pyruvic Acid in Aqueous Solutions. *Russ. Chem. Bull.* **2009**, *58* (9), 1828–1836. https://doi.org/10.1007/s11172-009-0249-2.
(36) Abel, B.; Assmann, J.; Buback, M.; Grimm, C.; Kling, M.; Schmatz, S.; Schroeder, J.; Witte, T. Ultrafast Decarboxylation of Carbonyloxy Radicals: Influence of Molecular Structure. *J. Phys. Chem. A* **2003**, *107* (45), 9499–9510. https://doi.org/10.1021/jp0350823.
(37) Bockman, T. M.; Hubig, S. M.; Kochi, J. K. Direct Observation of Ultrafast Decarboxylation of Acyloxy Radicals via Photoinduced Electron Transfer in Carboxylate Ion Pairs. *J. Org. Chem.* **1997**, *62* (7), 2210–2221. https://doi.org/10.1021/jo9617833.
(38) Hilborn, J. W.; Pincock, J. A. Rates of Decarboxylation of Acyloxy Radicals Formed in the Photocleavage of Substituted 1-Naphthylmethyl Alkanoates. *J. Am. Chem. Soc.* **1991**, *113* (7), 2683–2686. https://doi.org/10.1021/ja00007a049.
(39) Sonntag, C. von; Schuchmann, H.-P. The Elucidation of Peroxyl Radical Reactions in Aqueous Solution with the Help of Radiation-Chemical Methods. *Angew. Chem. Int. Ed. Engl.* **1991**, *30* (10), 1229–1253. https://doi.org/10.1002/anie.199112291.
(40) George, C.; Ammann, M.; D'Anna, B.; Donaldson, D. J.; Nizkorodov, S. A. Heterogeneous Photochemistry in the Atmosphere. *Chem. Rev.* **2015**, *115* (10), 4218–4258. https://doi.org/10.1021/cr500648z.
(41) Dou, J.; Alpert, P. A.; Corral Arroyo, P.; Luo, B.; Schneider, F.; Xto, J.; Huthwelker, T.; Borca, C. N.; Henzler, K. D.; Raabe, J.; Watts, B.; Herrmann, H.; Peter, T.; Ammann, M.; Krieger, U. K. Photochemical Degradation of Iron(III) Citrate/Citric Acid Aerosol Quantified with the Combination of Three Complementary Experimental Techniques and a Kinetic Process Model. *Atmospheric Chem. Phys.* **2021**, *21* (1), 315–338. https://doi.org/10.5194/acp-21-315-2021.
(42) Zuo, Y.; Hoigne, J. Formation of Hydrogen Peroxide and Depletion of Oxalic Acid in Atmospheric Water by Photolysis of Iron(III)-Oxalato Complexes. *Environ. Sci. Technol.* **1992**, *26* (5), 1014–1022. https://doi.org/10.1021/es00029a022.
(43) Zepp, R. G.; Faust, B. C.; Hoigne, J. Hydroxyl Radical Formation in Aqueous Reactions (PH 3-8) of Iron(II) with Hydrogen Peroxide: The Photo-Fenton Reaction. *Environ. Sci. Technol.* **1992**, *26* (2), 313–319. https://doi.org/10.1021/es00026a011.
(44) Balmer, M. E.; Sulzberger, B. Atrazine Degradation in Irradiated Iron/Oxalate Systems: Effects of PH and Oxalate. *Environ. Sci. Technol.* **1999**, *33* (14), 2418–2424. https://doi.org/10.1021/es9808705.
(45) Southworth, B. A.; Voelker, B. M. Hydroxyl Radical Production via the Photo-Fenton Reaction in the Presence of Fulvic Acid. *Environ. Sci. Technol.* **2003**, *37* (6), 1130–1136. https://doi.org/10.1021/es020757l.

(46) Fenton, H. J. H. LXXIII.—Oxidation of Tartaric Acid in Presence of Iron. *J. Chem. Soc. Trans.* **1894**, *65* (0), 899–910. https://doi.org/10.1039/CT8946500899.
(47) Zhang, C.; Wang, L.; Wu, F.; Deng, N. Quantitation of Hydroxyl Radicals from Photolysis of Fe(III)-Citrate Complexes in Aerobic Water (5 Pp). *Environ. Sci. Pollut. Res.* **2006**, *13* (3), 156–160. https://doi.org/10.1065/espr2005.10.287.
(48) Kim, S.-M.; Vogelpohl, A. Degradation of Organic Pollutants by the Photo-Fenton-Process. *Chem. Eng. Technol.* **1998**, *21* (2), 187–191. https://doi.org/10.1002/(SICI)1521-4125(199802)21:2<187::AID-CEAT187>3.0.CO;2-H.
(49) Sun, Yunfu.; Pignatello, J. J. Activation of Hydrogen Peroxide by Iron(III) Chelates for Abiotic Degradation of Herbicides and Insecticides in Water. *J. Agric. Food Chem.* **1993**, *41* (2), 308–312. https://doi.org/10.1021/jf00026a034.
(50) Fukushima, M.; Tatsumi, K. Degradation Pathways of Pentachlorophenol by Photo-Fenton Systems in the Presence of Iron(III), Humic Acid, and Hydrogen Peroxide. *Environ. Sci. Technol.* **2001**, *35* (9), 1771–1778. https://doi.org/10.1021/es001088j.
(51) Marchetti, B.; Karsili, T. N. V.; Ashfold, M. N. R. Exploring Norrish Type I and Type II Reactions: An Ab Initio Mechanistic Study Highlighting Singlet-State Mediated Chemistry. *Phys. Chem. Chem. Phys.* **2019**, *21* (26), 14418–14428. https://doi.org/10.1039/C8CP07292B.
(52) Norrish, R. G. W.; Appleyard, M. E. S. 191. Primary Photochemical Reactions. Part IV. Decomposition of Methyl Ethyl Ketone and Methyl Butyl Ketone. *J. Chem. Soc. Resumed* **1934**, No. 0, 874–880. https://doi.org/10.1039/JR9340000874.
(53) Pitts, J. N.; Blacet, F. E. METHYL ETHYL KETONE PHOTOCHEMICAL PROCESSES. *J. Am. Chem. Soc.* **1950**, *72* (6), 2810–2811. https://doi.org/10.1021/ja01162a544.
(54) Norrish, R. G. W.; Bamford, C. H. Photo-Decomposition of Aldehydes and Ketones. *Nature* **1937**, *140* (3535), 195–196. https://doi.org/10.1038/140195b0.
(55) Alpert, P. A.; Dou, J.; Corral Arroyo, P.; Schneider, F.; Xto, J.; Luo, B.; Peter, T.; Huthwelker, T.; Borca, C. N.; Henzler, K. D.; Schaefer, T.; Herrmann, H.; Raabe, J.; Watts, B.; Krieger, U. K.; Ammann, M. Photolytic Radical Persistence Due to Anoxia in Viscous Aerosol Particles. *Nat. Commun.* **2021**, *12* (1), 1769. https://doi.org/10.1038/s41467-021-21913-x.
(56) Zhang, Y.; Xie, H. Photomineralization and Photomethanification of Dissolved Organic Matter in Saguenay River Surface Water. *Biogeosciences* **2015**, *12* (22), 6823–6836. https://doi.org/10.5194/bg-12-6823-2015.
(57) Borduas-Dedekind, N.; Ossola, R.; David, R. O.; Boynton, L. S.; Weichlinger, V.; Kanji, Z. A.; McNeill, K. Photomineralization Mechanism Changes the Ability of Dissolved Organic Matter to Activate Cloud Droplets and to Nucleate Ice Crystals. *Atmospheric Chem. Phys.* **2019**, *19* (19), 12397–12412. https://doi.org/10.5194/acp-19-12397-2019.
(58) Barbeau, K.; Moffett, J. W. Laboratory and Field Studies of Colloidal Iron Oxide Dissolution as Mediated by Phagotrophy and Photolysis. *Limnol. Oceanogr.* **2000**, *45* (4), 827–835. https://doi.org/10.4319/lo.2000.45.4.0827.
(59) Wells, M. L.; Mayer, L. M.; Donard, O. F. X.; de Souza Sierra, M. M.; Ackelson, S. G. The Photolysis of Colloidal Iron in the Oceans. *Nature* **1991**, *353* (6341), 248–250. https://doi.org/10.1038/353248a0.
(60) Chen, X.; Ye, X.; Chu, W.; Olk, D. C.; Cao, X.; Schmidt-Rohr, K.; Zhang, L.; Thompson, M. L.; Mao, J.; Gao, H. Formation of Char-Like, Fused-Ring Aromatic Structures from a Nonpyrogenic Pathway during Decomposition of Wheat Straw. *J. Agric. Food Chem.* **2020**, *68* (9), 2607–2614. https://doi.org/10.1021/acs.jafc.9b06037.
(61) Abida, O.; Kolar, M.; Jirkovsky, J.; Mailhot, G. Degradation of 4-Chlorophenol in Aqueous Solution Photoinduced by Fe(III)–Citrate Complex. *Photochem. Photobiol. Sci.* **2012**, *11* (5), 794–802. https://doi.org/10.1039/C2PP05358F.

(62) Faust, B. C.; Zepp, R. G. Photochemistry of Aqueous Iron(III)-Polycarboxylate Complexes: Roles in the Chemistry of Atmospheric and Surface Waters. *Environ. Sci. Technol.* **1993**, *27* (12), 2517–2522. https://doi.org/10.1021/es00048a032.
(63) Arroyo, P. C.; Malecha, K. T.; Ammann, M.; Nizkorodov, S. A. Influence of Humidity and Iron(III) on Photodegradation of Atmospheric Secondary Organic Aerosol Particles. *Phys. Chem. Chem. Phys.* **2018**, *20* (47), 30021–30031. https://doi.org/10.1039/C8CP03981J.
(64) Aiona, P. K.; Lee, H. J.; Leslie, R.; Lin, P.; Laskin, A.; Laskin, J.; Nizkorodov, S. A. Photochemistry of Products of the Aqueous Reaction of Methylglyoxal with Ammonium Sulfate. *ACS Earth Space Chem.* **2017**, *1* (8), 522–532. https://doi.org/10.1021/acsearthspacechem.7b00075.
(65) Fleming, L. T.; Lin, P.; Roberts, J. M.; Selimovic, V.; Yokelson, R.; Laskin, J.; Laskin, A.; Nizkorodov, S. A. Molecular Composition and Photochemical Lifetimes of Brown Carbon Chromophores in Biomass Burning Organic Aerosol. *Atmospheric Chem. Phys.* **2020**, *20* (2), 1105–1129. https://doi.org/10.5194/acp-20-1105-2020.
(66) Lin, P.; Fleming, L. T.; Nizkorodov, S. A.; Laskin, J.; Laskin, A. Comprehensive Molecular Characterization of Atmospheric Brown Carbon by High Resolution Mass Spectrometry with Electrospray and Atmospheric Pressure Photoionization. *Anal. Chem.* **2018**, *90* (21), 12493–12502. https://doi.org/10.1021/acs.analchem.8b02177.
(67) Lavi, A.; Lin, P.; Bhaduri, B.; Carmieli, R.; Laskin, A.; Rudich, Y. Characterization of Light-Absorbing Oligomers from Reactions of Phenolic Compounds and Fe(III). *ACS Earth Space Chem.* **2017**, *1* (10), 637–646. https://doi.org/10.1021/acsearthspacechem.7b00099.
(68) Budisulistiorini, S. H.; Riva, M.; Williams, M.; Chen, J.; Itoh, M.; Surratt, J. D.; Kuwata, M. Light-Absorbing Brown Carbon Aerosol Constituents from Combustion of Indonesian Peat and Biomass. *Environ. Sci. Technol.* **2017**, *51* (8), 4415–4423. https://doi.org/10.1021/acs.est.7b00397.
(69) Lin, Y.-H.; Budisulistiorini, S. H.; Chu, K.; Siejack, R. A.; Zhang, H.; Riva, M.; Zhang, Z.; Gold, A.; Kautzman, K. E.; Surratt, J. D. Light-Absorbing Oligomer Formation in Secondary Organic Aerosol from Reactive Uptake of Isoprene Epoxydiols. *Environ. Sci. Technol.* **2014**, *48* (20), 12012–12021. https://doi.org/10.1021/es503142b.
(70) West, C. P.; Hettiyadura, A. P. S.; Darmody, A.; Mahamuni, G.; Davis, J.; Novosselov, I.; Laskin, A. Molecular Composition and the Optical Properties of Brown Carbon Generated by the Ethane Flame. *ACS Earth Space Chem.* **2020**, *4* (7), 1090–1103. https://doi.org/10.1021/acsearthspacechem.0c00095.
(71) Siemens, K.; Morales, A.; He, Q.; Li, C.; Hettiyadura, A. P. S.; Rudich, Y.; Laskin, A. Molecular Analysis of Secondary Brown Carbon Produced from the Photooxidation of Naphthalene. *Environ. Sci. Technol.* **2022**, *56* (6), 3340–3353. https://doi.org/10.1021/acs.est.1c03135.
(72) Lee, H. J. (Julie); Aiona, P. K.; Laskin, A.; Laskin, J.; Nizkorodov, S. A. Effect of Solar Radiation on the Optical Properties and Molecular Composition of Laboratory Proxies of Atmospheric Brown Carbon. *Environ. Sci. Technol.* **2014**, *48* (17), 10217–10226. https://doi.org/10.1021/es502515r.
(73) Silva, A. M. N.; Kong, X.; Parkin, M. C.; Cammack, R.; Hider, R. C. Iron(Iii) Citrate Speciation in Aqueous Solution. *Dalton Trans.* **2009**, No. 40, 8616. https://doi.org/10.1039/b910970f.
(74) Gautier-Luneau, I.; Merle, C.; Phanon, D.; Lebrun, C.; Biaso, F.; Serratrice, G.; Pierre, J.-L. New Trends in the Chemistry of Iron(III) Citrate Complexes: Correlations between X-Ray Structures and Solution Species Probed by Electrospray Mass Spectrometry and Kinetics of Iron Uptake from Citrate by Iron Chelators. *Chem. – Eur. J.* **2005**, *11* (7), 2207–2219. https://doi.org/10.1002/chem.200401087.
(75) Lehóczki, T.; Józsa, É.; Ősz, K. Ferrioxalate Actinometry with Online Spectrophotometric Detection. *J. Photochem. Photobiol. Chem.* **2013**, *251*, 63–68. https://doi.org/10.1016/j.jphotochem.2012.10.005.

(76) Stucki, J. W. The Quantitative Assay of Minerals for Fe2+ and Fe3+ Using 1,10-Phenanthroline: II. A Photochemical Method. *Soil Sci. Soc. Am. J.* **1981**, *45* (3), 638–641. https://doi.org/10.2136/sssaj1981.03615995004500030040x.
(77) Stucki, J. W.; Anderson, W. L. The Quantitative Assay of Minerals for Fe2+ and Fe3+ Using 1,10-Phenanthroline: I. Sources of Variability. *Soil Sci. Soc. Am. J.* **1981**, *45* (3), 633–637. https://doi.org/10.2136/sssaj1981.03615995004500030039x.
(78) Greco, G.; Letzel, T. Main Interactions and Influences of the Chromatographic Parameters in HILIC Separations. *J. Chromatogr. Sci.* **2013**, *51* (7), 684–693. https://doi.org/10.1093/chromsci/bmt015.
(79) Buszewski, B.; Noga, S. Hydrophilic Interaction Liquid Chromatography (HILIC)—a Powerful Separation Technique. *Anal. Bioanal. Chem.* **2012**, *402* (1), 231–247. https://doi.org/10.1007/s00216-011-5308-5.
(80) AlChoubassi, G.; Aszyk, J.; Pisarek, P.; Bierla, K.; Ouerdane, L.; Szpunar, J.; Lobinski, R. Advances in Mass Spectrometry for Iron Speciation in Plants. *TrAC Trends Anal. Chem.* **2018**, *104*, 77–86. https://doi.org/10.1016/j.trac.2017.11.006.
(81) Spagou, K.; Tsoukali, H.; Raikos, N.; Gika, H.; Wilson, I. D.; Theodoridis, G. Hydrophilic Interaction Chromatography Coupled to MS for Metabonomic/Metabolomic Studies. *J. Sep. Sci.* **2010**, *33* (6–7), 716–727. https://doi.org/10.1002/jssc.200900803.
(82) Dell'mour, M.; Schenkeveld, W.; Oburger, E.; Fischer, L.; Kraemer, S.; Puschenreiter, M.; Lämmerhofer, M.; Koellensperger, G.; Hann, S. Analysis of Iron-Phytosiderophore Complexes in Soil Related Samples: LC-ESI-MS/MS versus CE-MS. *ELECTROPHORESIS* **2012**, *33* (4), 726–733. https://doi.org/10.1002/elps.201100466.
(83) Tsednee, M.; Mak, Y.-W.; Chen, Y.-R.; Yeh, K.-C. A Sensitive LC-ESI-Q-TOF-MS Method Reveals Novel Phytosiderophores and Phytosiderophore–Iron Complexes in Barley. *New Phytol.* **2012**, *195* (4), 951–961. https://doi.org/10.1111/j.1469-8137.2012.04206.x.
(84) Rellán-Álvarez, R.; Giner-Martínez-Sierra, J.; Orduna, J.; Orera, I.; Rodríguez-Castrillón, J. Á.; García-Alonso, J. I.; Abadía, J.; Álvarez-Fernández, A. Identification of a Tri-Iron(III), Tri-Citrate Complex in the Xylem Sap of Iron-Deficient Tomato Resupplied with Iron: New Insights into Plant Iron Long-Distance Transport. *Plant Cell Physiol.* **2010**, *51* (1), 91–102. https://doi.org/10.1093/pcp/pcp170.
(85) Xuan, Y.; Scheuermann, E. B.; Meda, A. R.; Hayen, H.; von Wirén, N.; Weber, G. Separation and Identification of Phytosiderophores and Their Metal Complexes in Plants by Zwitterionic Hydrophilic Interaction Liquid Chromatography Coupled to Electrospray Ionization Mass Spectrometry. *J. Chromatogr. A* **2006**, *1136* (1), 73–81. https://doi.org/10.1016/j.chroma.2006.09.060.
(86) Pluskal, T.; Castillo, S.; Villar-Briones, A.; Orešič, M. MZmine 2: Modular Framework for Processing, Visualizing, and Analyzing Mass Spectrometry-Based Molecular Profile Data. *BMC Bioinformatics* **2010**, *11* (1), 395. https://doi.org/10.1186/1471-2105-11-395.
(87) Kuhl, C.; Tautenhahn, R.; Böttcher, C.; Larson, T. R.; Neumann, S. CAMERA: An Integrated Strategy for Compound Spectra Extraction and Annotation of LC/MS Data Sets. *Anal. Chem.* **2012**, *84* (1), 283–289. https://doi.org/10.1021/ac202450g.
(88) Myers, O. D.; Sumner, S. J.; Li, S.; Barnes, S.; Du, X. One Step Forward for Reducing False Positive and False Negative Compound Identifications from Mass Spectrometry Metabolomics Data: New Algorithms for Constructing Extracted Ion Chromatograms and Detecting Chromatographic Peaks. *Anal. Chem.* **2017**, *89* (17), 8696–8703. https://doi.org/10.1021/acs.analchem.7b00947.
(89) Jaitly, N.; Mayampurath, A.; Littlefield, K.; Adkins, J. N.; Anderson, G. A.; Smith, R. D. Decon2LS: An Open-Source Software Package for Automated Processing and Visualization of High Resolution Mass Spectrometry Data. *BMC Bioinformatics* **2009**, *10* (1), 87. https://doi.org/10.1186/1471-2105-10-87.

(90) Roach, P. J.; Laskin, J.; Laskin, A. Higher-Order Mass Defect Analysis for Mass Spectra of Complex Organic Mixtures. *Anal. Chem.* **2011**, *83* (12), 4924–4929. https://doi.org/10.1021/ac200654j.
(91) Vetter, W. F. W. McLafferty, F. Turecek. Interpretation of Mass Spectra. Fourth Edition (1993). University Science Books, Mill Valley, California. *Biol. Mass Spectrom.* **1994**, *23* (6), 379–379. https://doi.org/10.1002/bms.1200230614.
(92) Chen, Y.; Bond, T. C. Light Absorption by Organic Carbon from Wood Combustion. *Atmospheric Chem. Phys.* **2010**, *10* (4), 1773–1787. https://doi.org/10.5194/acp-10-1773-2010.
(93) Kirchstetter, T. W.; Novakov, T.; Hobbs, P. V. Evidence That the Spectral Dependence of Light Absorption by Aerosols Is Affected by Organic Carbon. *J. Geophys. Res. Atmospheres* **2004**, *109* (D21). https://doi.org/10.1029/2004JD004999.
(94) Hettiyadura, A. P. S.; Laskin, A. Quantitative Analysis of Polycyclic Aromatic Hydrocarbons Using High-Performance Liquid Chromatography-Photodiode Array-High-Resolution Mass Spectrometric Detection Platform Coupled to Electrospray and Atmospheric Pressure Photoionization Sources. *J. Mass Spectrom.* **2022**, *57* (2), e4804. https://doi.org/10.1002/jms.4804.
(95) Hettiyadura, A. P. S.; Garcia, V.; Li, C.; West, C. P.; Tomlin, J.; He, Q.; Rudich, Y.; Laskin, A. Chemical Composition and Molecular-Specific Optical Properties of Atmospheric Brown Carbon Associated with Biomass Burning. *Environ. Sci. Technol.* **2021**, *55* (4), 2511–2521. https://doi.org/10.1021/acs.est.0c05883.
(96) Krause, N.; Kuhn, S.; Frotscher, E.; Nikels, F.; Hawe, A.; Garidel, P.; Menzen, T. Oil-Immersion Flow Imaging Microscopy for Quantification and Morphological Characterization of Submicron Particles in Biopharmaceuticals. *AAPS J.* **2021**, *23* (1), 13. https://doi.org/10.1208/s12248-020-00547-9.
(97) Hasberg, A. K. M.; Bijaksana, S.; Held, P.; Just, J.; Melles, M.; Morlock, M. A.; Opitz, S.; Russell, J. M.; Vogel, H.; Wennrich, V. Modern Sedimentation Processes in Lake Towuti, Indonesia, Revealed by the Composition of Surface Sediments. *Sedimentology* **2019**, *66* (2), 675–698. https://doi.org/10.1111/sed.12503.
(98) Seraghni, N.; Belattar, S.; Mameri, Y.; Debbache, N.; Sehili, T. Fe(III)-Citrate-Complex-Induced Photooxidation of 3-Methylphenol in Aqueous Solution https://www.hindawi.com/journals/ijp/2012/630425/ (accessed 2021 -03 -02). https://doi.org/10.1155/2012/630425.
(99) Ruales-Lonfat, C.; Barona, J. F.; Sienkiewicz, A.; Vélez, J.; Benítez, L. N.; Pulgarín, C. Bacterial Inactivation with Iron Citrate Complex: A New Source of Dissolved Iron in Solar Photo-Fenton Process at near-Neutral and Alkaline PH. *Appl. Catal. B Environ.* **2016**, *180*, 379–390. https://doi.org/10.1016/j.apcatb.2015.06.030.
(100) Ogi, Y.; Obara, Y.; Katayama, T.; Suzuki, Y.-I.; Liu, S. Y.; Bartlett, N. C.-M.; Kurahashi, N.; Karashima, S.; Togashi, T.; Inubushi, Y.; Ogawa, K.; Owada, S.; Rubešová, M.; Yabashi, M.; Misawa, K.; Slavíček, P.; Suzuki, T. Ultraviolet Photochemical Reaction of [Fe(III)(C2O4)3]3− in Aqueous Solutions Studied by Femtosecond Time-Resolved X-Ray Absorption Spectroscopy Using an X-Ray Free Electron Laser. *Struct. Dyn.* **2015**, *2* (3), 034901. https://doi.org/10.1063/1.4918803.
(101) Dekkiche, B. A.; Seraghni, N.; Debbache, N.; Ghoul, I.; Sehili, T. Effect of Natural and Artificial Light on Fe(III) Organic Complexes Photolysis: Case of Fe (III)-Malonate and Fe(III)-Malate. *Int. J. Chem. React. Eng.* **2019**, *17* (2). https://doi.org/10.1515/ijcre-2018-0106.
(102) Wang, L.; Zhang, C.; Mestankova, H.; Wu, F.; Deng, N.; Pan, G.; Bolte, M.; Mailhot, G. Photoinduced Degradation of 2,4-Dichlorophenol in Water: Influence of Various Fe(III) Carboxylates. *Photochem. Photobiol. Sci.* **2009**, *8* (7), 1059–1065. https://doi.org/10.1039/B902607J.
(103) Fu, Z.; Chen, R. Study of Complexes of Tannic Acid with Fe(III) and Fe(II). *J. Anal. Methods Chem.* **2019**, *2019*, e3894571. https://doi.org/10.1155/2019/3894571.

(104) Thorarinsdottir, A. E.; Gaudette, A. I.; Harris, T. D. Spin-Crossover and High-Spin Iron(II) Complexes as Chemical Shift 19F Magnetic Resonance Thermometers. *Chem. Sci.* **2017**, *8* (3), 2448–2456. https://doi.org/10.1039/C6SC04287B.

(105) Baxendale, J. H.; Magee, J. The Photochemical Oxidation of Benzene in Aqueous Solution by Ferric Ion. *Trans. Faraday Soc.* **1955**, *51* (0), 205–213. https://doi.org/10.1039/TF9555100205.

(106) Moffett, J. W.; Zika, R. G. Reaction Kinetics of Hydrogen Peroxide with Copper and Iron in Seawater. *Environ. Sci. Technol.* **1987**, *21* (8), 804–810. https://doi.org/10.1021/es00162a012.

(107) Quici, N.; Morgada, M. E.; Gettar, R. T.; Bolte, M.; Litter, M. I. Photocatalytic Degradation of Citric Acid under Different Conditions: TiO2 Heterogeneous Photocatalysis against Homogeneous Photolytic Processes Promoted by Fe(III) and H2O2. *Appl. Catal. B Environ.* **2007**, *71* (3), 117–124. https://doi.org/10.1016/j.apcatb.2006.09.001.

(108) Waite, T. D.; Morel, F. M. Photoreductive Dissolution of Colloidal Iron Oxides in Natural Waters. *Environ. Sci. Technol.* **1984**, *18* (11), 860–868. https://doi.org/10.1021/es00129a010.

(109) Meng, X.; Ryu, J.; Kim, B.; Ko, S. Application of Iron Oxide as a PH-Dependent Indicator for Improving the Nutritional Quality. *Clin. Nutr. Res.* **2016**, *5* (3), 172–179. https://doi.org/10.7762/cnr.2016.5.3.172.

(110) Li, F.; Koopal, L.; Tan, W. Roles of Different Types of Oxalate Surface Complexes in Dissolution Process of Ferrihydrite Aggregates. *Sci. Rep.* **2018**, *8* (1), 2060. https://doi.org/10.1038/s41598-018-20401-5.

(111) Borer, P.; Hug, S. J.; Sulzberger, B.; Kraemer, S. M.; Kretzschmar, R. Photolysis of Citrate on the Surface of Lepidocrocite: An in Situ Attenuated Total Reflection Infrared Spectroscopy Study. *J. Phys. Chem. C* **2007**, *111* (28), 10560–10569. https://doi.org/10.1021/jp0685941.

(112) Lv, Y.; Liu, J.; Zhu, R.; Zhu, J.; Chen, Q.; Liang, X.; He, H. Photoreductive Dissolution of Iron (Hydr)Oxides and Its Geochemical Significance. *ACS Earth Space Chem.* **2022**. https://doi.org/10.1021/acsearthspacechem.1c00334.

(113) Silva, A. M. N.; Kong, X.; Parkin, M. C.; Cammack, R.; Hider, R. C. Iron(III) Citrate Speciation in Aqueous Solution. *Dalton Trans.* **2009**, No. 40, 8616–8625. https://doi.org/10.1039/B910970F.

(114) National Center for Biotechnology Information. "PubChem Compound Summary for CID 14298643, Ferrous Citrate" PubChem, Https://Pubchem.Ncbi.Nlm.Nih.Gov/Compound/Ferrous-Citrate. Accessed 18 December, 2020.

(115) Pierre, J. L.; Gautier-Luneau, I. Iron and Citric Acid: A Fuzzy Chemistry of Ubiquitous Biological Relevance. *Biometals* **2000**, *13* (1), 91–96. https://doi.org/10.1023/A:1009225701332.

(116) Königsberger, L.-C.; Königsberger, E.; May, P. M.; Hefter, G. T. Complexation of Iron(III) and Iron(II) by Citrate. Implications for Iron Speciation in Blood Plasma. *J. Inorg. Biochem.* **2000**, *78* (3), 175–184. https://doi.org/10.1016/S0162-0134(99)00222-6.

(117) Pham, A. N.; Waite, T. D. Oxygenation of Fe(II) in the Presence of Citrate in Aqueous Solutions at PH 6.0−8.0 and 25 °C: Interpretation from an Fe(II)/Citrate Speciation Perspective. *J. Phys. Chem. A* **2008**, *112* (4), 643–651. https://doi.org/10.1021/jp077219l.

(118) Harris, D. C.; Aisen, P. Facilitation of Fe(II) Antoxidation by Fe(III) Complexing Agents. *Biochim. Biophys. Acta BBA - Gen. Subj.* **1973**, *329* (1), 156–158. https://doi.org/10.1016/0304-4165(73)90019-6.

(119) Liu, M. J.; Wiegel, A. A.; Wilson, K. R.; Houle, F. A. Aerosol Fragmentation Driven by Coupling of Acid–Base and Free-Radical Chemistry in the Heterogeneous Oxidation of Aqueous Citric Acid by OH Radicals. *J. Phys. Chem. A* **2017**, *121* (31), 5856–5870. https://doi.org/10.1021/acs.jpca.7b04892.

(120) Moharregh-Khiabani, D.; Linker, R. A.; Gold, R.; Stangel, M. Fumaric Acid and Its Esters: An Emerging Treatment for Multiple Sclerosis. *Curr. Neuropharmacol.* **2009**, *7* (1), 60–64. https://doi.org/10.2174/157015909787602788.

(121) Ponczek, M.; Hayeck, N.; Emmelin, C.; George, C. Heterogeneous Photochemistry of Dicarboxylic Acids on Mineral Dust. *Atmos. Environ.* **2019**, *212*, 262–271. https://doi.org/10.1016/j.atmosenv.2019.05.032.

(122) Mazurek, A.; Jamroz, J. Precision of Dehydroascorbic Acid Quantitation with the Use of the Subtraction Method – Validation of HPLC–DAD Method for Determination of Total Vitamin C in Food. *Food Chem.* **2015**, *173*, 543–550. https://doi.org/10.1016/j.foodchem.2014.10.065.

(123) Dewhirst, R. A.; Fry, S. C. The Oxidation of Dehydroascorbic Acid and 2,3-Diketogulonate by Distinct Reactive Oxygen Species. *Biochem. J.* **2018**, *475* (21), 3451–3470. https://doi.org/10.1042/BCJ20180688.

(124) Siegmann, K.; Sattler, K. Formation Mechanism for Polycyclic Aromatic Hydrocarbons in Methane Flames. *J. Chem. Phys.* **2000**, *112* (2), 698–709. https://doi.org/10.1063/1.480648.

(125) Cain, J.; Laskin, A.; Kholghy, M. R.; Thomson, M. J.; Wang, H. Molecular Characterization of Organic Content of Soot along the Centerline of a Coflow Diffusion Flame. *Phys. Chem. Chem. Phys.* **2014**, *16* (47), 25862–25875. https://doi.org/10.1039/C4CP03330B.

(126) Saleh, R. From Measurements to Models: Toward Accurate Representation of Brown Carbon in Climate Calculations. *Curr. Pollut. Rep.* **2020**, *6* (2), 90–104. https://doi.org/10.1007/s40726-020-00139-3.

(127) Zhou, Y.; West, C. P.; Hettiyadura, A. P. S.; Niu, X.; Wen, H.; Cui, J.; Shi, T.; Pu, W.; Wang, X.; Laskin, A. Measurement Report: Molecular Composition, Optical Properties, and Radiative Effects of Water-Soluble Organic Carbon in Snowpack Samples from Northern Xinjiang, China. *Atmospheric Chem. Phys.* **2021**, *21* (11), 8531–8555. https://doi.org/10.5194/acp-21-8531-2021.

(128) Alexander, D. T. L.; Crozier, P. A.; Anderson, J. R. Brown Carbon Spheres in East Asian Outflow and Their Optical Properties. *Science* **2008**, *321* (5890), 833–836. https://doi.org/10.1126/science.1155296.

(129) Misovich, M. V.; Hettiyadura, A. P. S.; Jiang, W.; Zhang, Q.; Laskin, A. Molecular-Level Study of the Photo-Oxidation of Aqueous-Phase Guaiacyl Acetone in the Presence of 3C*: Formation of Brown Carbon Products. *ACS Earth Space Chem.* **2021**, *5* (8), 1983–1996. https://doi.org/10.1021/acsearthspacechem.1c00103.

(130) Zangmeister, C. D.; You, R.; Lunny, E. M.; Jacobson, A. E.; Okumura, M.; Zachariah, M. R.; Radney, J. G. Measured In-Situ Mass Absorption Spectra for Nine Forms of Highly-Absorbing Carbonaceous Aerosol. *Carbon* **2018**, *136*, 85–93. https://doi.org/10.1016/j.carbon.2018.04.057.

(131) Miles, C. J.; Brezonik, P. L. Oxygen Consumption in Humic-Colored Waters by a Photochemical Ferrous-Ferric Catalytic Cycle. *Environ. Sci. Technol.* **1981**, *15* (9), 1089–1095. https://doi.org/10.1021/es00091a010.

(132) Byrne, J. M.; Klueglein, N.; Pearce, C.; Rosso, K. M.; Appel, E.; Kappler, A. Redox Cycling of Fe(II) and Fe(III) in Magnetite by Fe-Metabolizing Bacteria. *Science* **2015**, *347* (6229), 1473–1476. https://doi.org/10.1126/science.aaa4834.

(133) Emmenegger, L.; Schönenberger, R.; Sigg, L.; Sulzberger, B. Light-Induced Redox Cycling of Iron in Circumneutral Lakes. *Limnol. Oceanogr.* **2001**, *46* (1), 49–61. https://doi.org/10.4319/lo.2001.46.1.0049.

(134) Cwiertny, D. M.; Young, M. A.; Grassian, V. H. Chemistry and Photochemistry of Mineral Dust Aerosol. *Annu. Rev. Phys. Chem.* **2008**, *59* (1), 27–51. https://doi.org/10.1146/annurev.physchem.59.032607.093630.

(135) Siefert, R. L.; Pehkonen, S. O.; Erel, Y.; Hoffmann, M. R. Iron Photochemistry of Aqueous Suspensions of Ambient Aerosol with Added Organic Acids. *Geochim. Cosmochim. Acta* **1994**, *58* (15), 3271–3279. https://doi.org/10.1016/0016-7037(94)90055-8.

(136) Pu, W.; Wang, X.; Wei, H.; Zhou, Y.; Shi, J.; Hu, Z.; Jin, H.; Chen, Q. Properties of Black Carbon and Other Insoluble Light-Absorbing Particles in Seasonal Snow of Northwestern China. *The Cryosphere* **2017**, *11* (3), 1213–1233. https://doi.org/10.5194/tc-11-1213-2017.

(137) Shi, T.; Cui, J.; Chen, Y.; Zhou, Y.; Pu, W.; Xu, X.; Chen, Q.; Zhang, X.; Wang, X. Enhanced Light Absorption and Reduced Snow Albedo Due to Internally Mixed Mineral Dust in Grains of Snow. *Atmospheric Chem. Phys.* **2021**, *21* (8), 6035–6051. https://doi.org/10.5194/acp-21-6035-2021.

(138) Zhou, Y.; West, C. P.; Hettiyadura, A. P. S.; Pu, W.; Shi, T.; Niu, X.; Wen, H.; Cui, J.; Wang, X.; Laskin, A. Molecular Characterization of Water-Soluble Brown Carbon Chromophores in Snowpack from Northern Xinjiang, China. *Environ. Sci. Technol.* **2022**, *56* (7), 4173–4186. https://doi.org/10.1021/acs.est.1c07972.